Effects of Lattice Strain in Silicon Double Crystal Monochromators

Master's Thesis
Division of Synchrotron Radiation Research

Johan Eckdahl

Supervisors: Peter Sondhauss, Sverker Werin

May 7, 2018

LUND
UNIVERSITY

Abstract

Silicon double crystal monochromators are standard in modern synchrotron hard X-ray beamlines. Their role is reducing a polychromatic photon beam to a small range of wavelengths, typically within a bandwidth of 0.01-0.1%. These monochromators work through the principle of Bragg diffraction where the crystal lattice spacing, photon energy and incident angle determines the reflectivity of the crystal. One must consider that the first crystal in the system receives an enormous heat load as it absorbs the vast majority of the beam power, which is in the kilowatt regime. The heat creates thermoelastic stress that warps the crystal surface and alters its lattice spacing. This paper investigates the effects of this on the reflected beam through the help of simulations. Calculations using COMSOL for finite element analysis of heat transport, thermal expansion, elastic strain, and deformation and SHADOW3 for ray tracing of radiation transfer were coordinated by a framework called MASH. First, a numerical study of diffraction in Si 111 and Si 333 with a uniform strain gradient was performed. Then hard X-ray sources of varying energies were used to study reflectivity in Si 111 and Si 333 for the cases of strained and unstrained crystals with or without deformation. Monochromator performance, i.e. the attenuation and bandwidth of the beam after monochromation, was recorded. Significance of the results is discussed and further study proposed.

Contents

1 Introduction

Hard X-ray beamlines at modern synchrotron facilities continue to expand their capabilities into the many fields of science. From medical imaging to nanoscience, X-ray measurement techniques are revolutionizing the way research is performed. These powerful beams must be kept in check in order to control radiation exposure to beamline components. Radiation takes a toll not only on their longevity, but on their performance. Of the optical components the monochromator is subject to receiving the highest power loads. This is due to the full spectrum of the beam source being incident upon its surface and only a small fraction of the power reflected further down stream. The majority of the power is deposited in the body of the monochromator and it thereby suffers performance losses as the deposited energy warps its structure. This has the potential result of erratic and severe attenuation. It is often hard to find the sources of these errors and easy to misplace blame. Therefore, by understanding with great detail the effects of these heat loads an engineer is better equipped in designing and troubleshooting a monochromating system.

Countless simulations of silicon monochromators have been performed providing a detailed look into their behavior under many different beamline conditions. However, to our knowledge no publication has described such simulations including all effects of lattice strain on the reflection profile.

A publication by Zhang et al. [1] studies surface deformation under heat load of silicon monochromating crystals. Simulations by the group agreed well with their experimental results, however a free parameter was used while curve fitting. It is desired to create a model fitting experimental results without the use of free parameters while also incorporating the effects of strain in the crystal lattice. The result will be novel methodology that will allow beamline scientists to more accurately predict the reflectivity of their monochromators.

The introduction continues with a description of a typical modern synchrotron facility followed by a brief introduction to MAX IV. Moving on to Section 2, a theoretical background will be built in order for the reader to develop an understanding for the physical phenomena exploited in this study. A section describing the simulation methodology follows. The specificity of the writing increases with a section covering the setup and execution of the simulations involved in the study. The penultimate section describes the results of the simulations and reveals the effects of crystal strain due to the varying of several beamline parameters. Finally, an outlook section wraps up this writing by looking at this study's results and its future growth.

1.1 Facility Overview

Most large, modern storage ring synchrotron radiation facilities share a general structure similar to that seen in Figure 1.1. The largest feature is the storage ring. The storage ring is a long pipe kept under ultra-high vacuum which houses small (order of microns) bunches of electrons circulating in the ring at close to the speed of light. The particles circulate until deliberately discarded or are inadvertently taken off course and collide with the ring wall. Circulation allows continued use of the electron beam for the facility over each pass. One can see that the main storage ring is not a perfect circle but a combination of bending and straight sections. In a bending section, magnets provide the crucial function of keeping the electrons on the path of the ring. These bending magnets also provide a source of light that can be used for experimentation. Although, most often this light is considered inferior to that provided by insertion devices. Insertion devices are found in the straight regions, known as "insertion regions", and provide extremely intense directed synchrotron radiation for use in experiments.

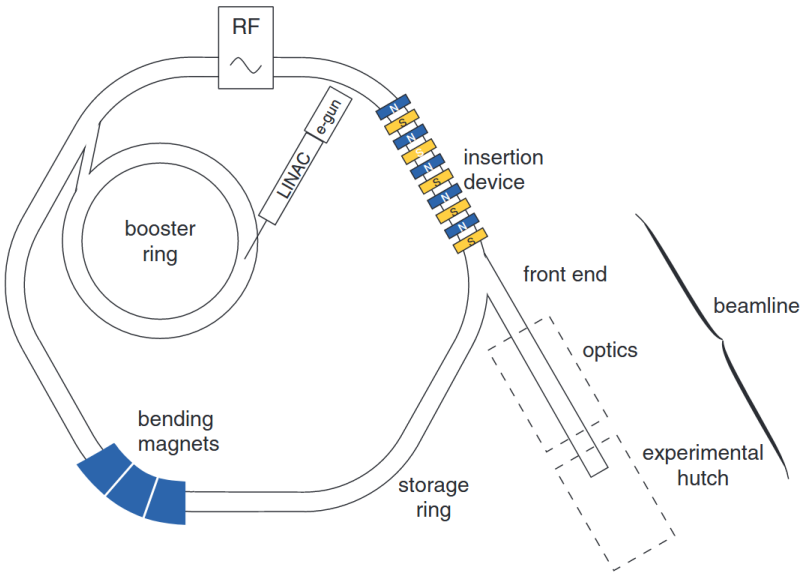

Figure 1.1: An overview of a typical synchrotron radiation facility [2]

Before entering the main storage ring electrons must be accelerated to a suitable energy for injection. The acceleration process begins in the electron gun where electrons are stripped from a cathode (e.g. by thermionic emission or the photoelectric effect) and accelerated by an electric field until they enter a large linear accelerator (LINAC). The LINAC is a series of cavities with an oscillating electromagnetic field typically within the radio to microwave range. The cavities are spaced precisely so that relativistic electrons will reach consecutive cavities when the electric field produces a positive acceleration. Electrons deviant to this pattern are either lost from the beam or are pushed towards a more favorable position. This results in the bunching of electrons which are separated by the wavelength of the cavity oscillations. At the end of the LINAC the beam can be inserted into a booster ring, or a series of booster rings, that increase the electron energies further. Finally the beam enters the main storage ring where it begins its work emitting quality light for experimental usage. Some facilities opt not to have booster rings and the final additions of energy after the LINAC occurs in the storage ring. Others inject at full energy from the LINAC into the storage ring where the energy is only maintained. In all situations the timing of the accelerating cavities in a ring (labeled RF in Figure 1.1) and strength of the field in the bending magnets is crucial to stable operation. Circulating electron bunches must maintain separation similar to that of wavelength of the cavity oscillations during energy ramping but also once they've reached their working energy in order to replenish power lost due to radiation emission. Bending magnet strength must be synchronized along with electron energy in order to keep the higher momentum particles on track. This synchronization is where the radiation earns its name.

As the light exits the insertion device and leaves the ring it encounters yet more complexities that serve its treatment. The first obstacle the light meets is the "front end". The front end conditions the raw beam for the optics further downstream. It consists of beam position monitors (BPM), apertures to define angular acceptance and filters that attenuate specific parts of the spectrum. In hard X-ray experiments it is most often crucial to remove the lower energy parts of the spectrum from the beam. These low energy photons interact strongly with matter and can damage or destroy beamline optics. This can be done by skimming off the lower energy contributions that are naturally found at angles higher off the beam axis and by depositing power from lower frequencies in materials suitable for attenuation.

After this conditioning the beam enters the optics section of the beamline. Here the beam meets focusing optics such as mirrors that are designed for the low grazing incidences required of X-ray reflection and which demand extremely smooth and accurately shaped surfaces. Monochromators of several types exist in the form of gratings, or other artificially generated periodic structures, or crystals with their natural lattice periodicity as a means for diffraction. A simple visual of an optical setup is seen in Figure 1.2. Simulation and experimentation with crystal monochromators is the main topic of this paper.

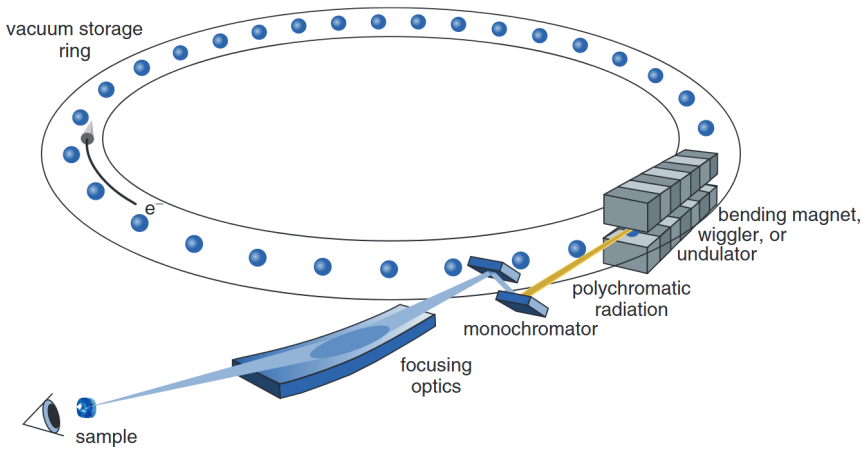

Figure 1.2: Diagram of monochromation and focusing of synchrotron light [2]

Finally, the beam enters an experimental hutch where it receives experiment specific conditioning and application to a sample. The detector stands ready to take the light in its final form and store it as data for analysis.

Further information on these topics will be given, as necessary, in following sections and appendices.

1.1.1 The MAX IV Facility

Simulations performed will have a focus on conditions found at the MAX IV synchrotron facility located in Lund, Sweden. The laboratory opened in 2015 and is currently the most brilliant storage ring based synchrotron light source [3]. It is still quite young, however, and both existing and planned beamlines are focused on refining their capabilities in preparation for an expected influx of visiting users in the coming years. The NanoMAX [4] and BioMAX [5] beamlines desire detailed simulations of their identical monochromators. This paper concerns itself with simulations of silicon double monochromator crystals under generic conditions but also has the end focus of performing specific simulations of the systems at these two beamlines. Methodology developed in these studies will be widely applicable and is intended to be used in the detailed design report for the planned MAX IV beamline ForMAX [6].

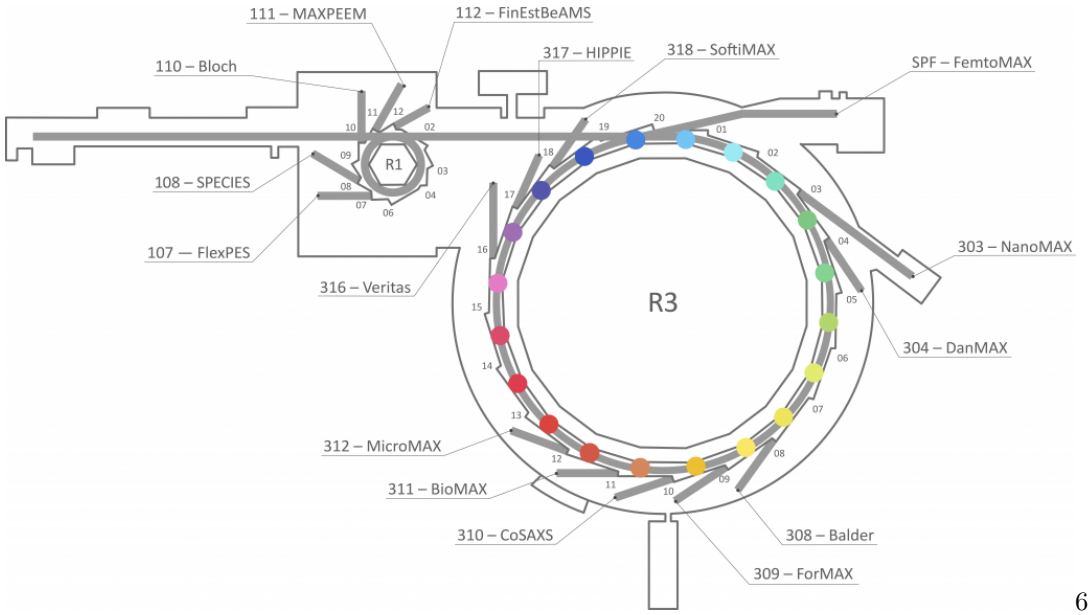

Figure 1.3: Planned or existing beamlines found around the circumference of the 1.5 GeV ring (left) and the 3 GeV ring (right) at the MAX IV facility [7]

2 Background

2.1 Synchrotron Radiation and Accelerator Technology

2.1.1 Beginnings

Synchrotron radiation is a form of electromagnetic radiation produced by the radial acceleration of charged relativistic particles. It is named after the synchrotron, a circular accelerator that increases the energy of a particle with each pass to maintain a desired particle energy. It was at a synchrotron where the discovery of synchrotron light occurred in 1948. That year Robert Langmuir and Herb Pollock observed a beam of light emanating from the newly built synchrotron at General Electric in Schenectady, New York. Initially considered a parasitic energy loss, the utility of the beams was soon discovered. Not long after, construction began of "second generation" synchrotrons defined by their design and dedication to producing intense beams of light.

Second generation facilities used the synchrotron radiation produced by electrons deflected by strong bending magnets. Bending magnets can be as simple as two magnetic poles creating a uniform magnetic field as seen in Figure 2.1. Magnets in modern facilities, however, can consist of superconducting coils, cryogenic systems and integrated quadrupole focusing magnets. Radial acceleration through the magnet produces a fan of light with horizontal width equaling the deflection angle of the electrons. The synchrotron radiation has a continuous spectrum with properties dependent on factors such as the magnetic field strength, electron energy and beam current. An example spectrum for a 1 GeV electron beam with 400 mA current and 1 T field strength was produced with an online calculator provided by the Lawrence Berkeley Laboratory [8] and seen in Figure 2.1. Note in the figure that the power output is nearly constant across a wide range of photon energies before it sharply drops off at the higher end. This means a bending magnet can act as a single source for experiments requiring large energy ranges. Due to the extensive width of the produced beam, a single bending magnet can provide for more than one experimental station.

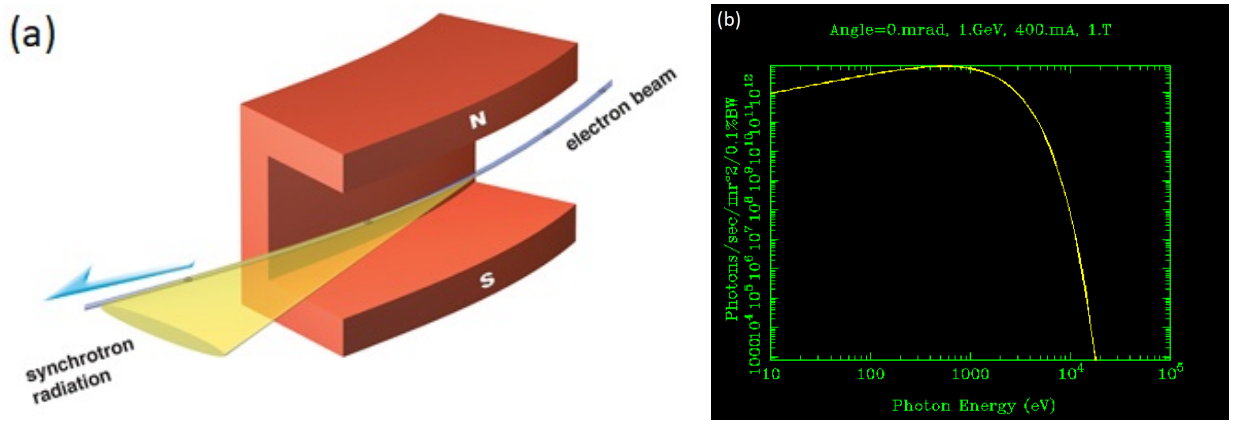

Figure 2.1: (a) simple bending magnet and emerging light [9] (b) example bending magnet spectrum generated by the Internet calculator in Reference [8]

2.1.2 Insertion Devices

New technologies were developed that dramatically boosted the capabilities of synchrotron light source facilities. Most significantly, so-called "insertion devices" were installed into the straight sections, or "insertion regions", of accelerator rings as seen in Figure 1.1. Insertion devices are a series of magnets placed single-file with alternating polarity. This alternating field causes charged particles to "wiggle" or "undulate" through the device. This type of acceleration creates extremely powerful and forward-boosted light. A schematic of an insertion device is shown in Figure 2.2.

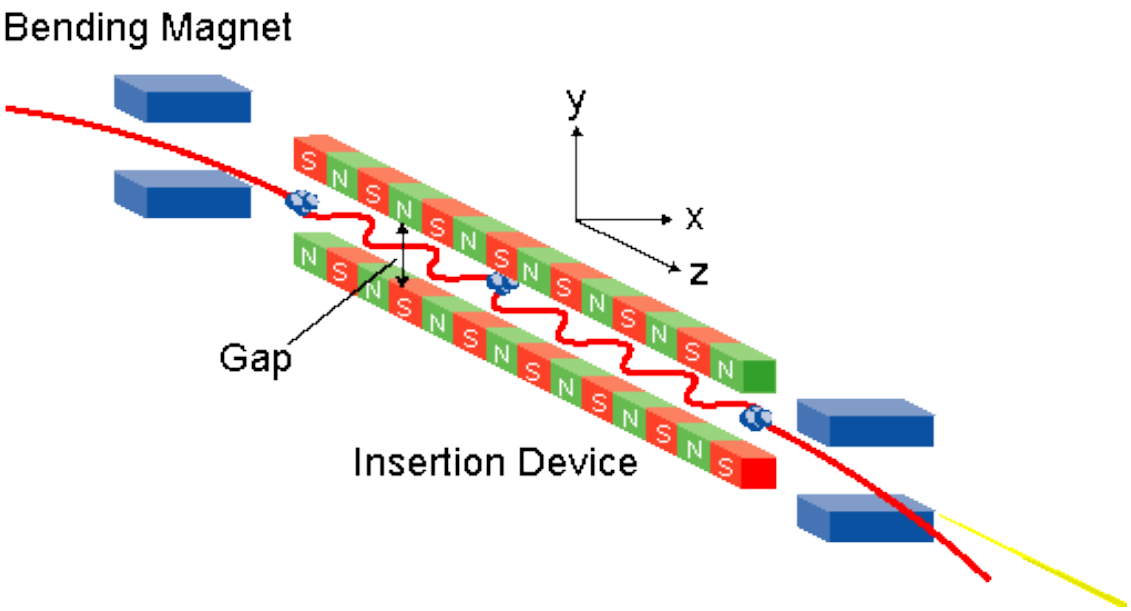

Figure 2.2: Schematic of an insertion device of a synchrotron light source as provided by Reference [10]

Unlike bending magnet radiation, that from an undulator is typically divided into several narrow peaks called harmonics. An insertion device is well described by its deflection parameter K, Equation (1), when inserted into the undulator equation given by Equation (2). K is given by

$$K = \frac{eB_0\lambda_u}{2\pi m_e c} \tag{1}$$

where e is the elementary charge, B_0 the maximum magnetic field, m_e the electron mass, c the speed of light and λ_u the period length of the insertion device. The undulator equation is given by

$$\lambda = \frac{\lambda_u}{2n\gamma^2}\left(1 + \frac{K^2}{2} + \theta^2\gamma^2\right) \tag{2}$$

where λ is the nth harmonic wavelength, λ_u the period length of the insertion device, n the harmonic as a natural number, $\gamma = E/m_e c^2$ the relativistic gamma factor of an electron, E is the relativistic electron energy, m_e the electron mass, c the speed of light, and θ the observation angle from the beam axis.

Inserting Equation (1) into (2) one can readily obtain the wavelengths and bandwidths of each of the harmonics at any observation angle.

With increasing K intensity is shifted towards the higher harmonics and the nearly muted even harmonics begin to appear in the spectrum as seen in Figure 2.3c. At K values higher still the spectral features begin to merge into to a shape similar to a bending magnet seen earlier, as demonstrated in Figure 2.3. The change is gradual and often an insertion device is classified as an undulator or wiggler based upon its K value. Undulator K values generally hover around 1 or less while those for wigglers are much higher, though this convention is often broken as naming is more a matter of describing the devices' intended function: providing sharp spectral lines or broader ones with a higher overall intensity.

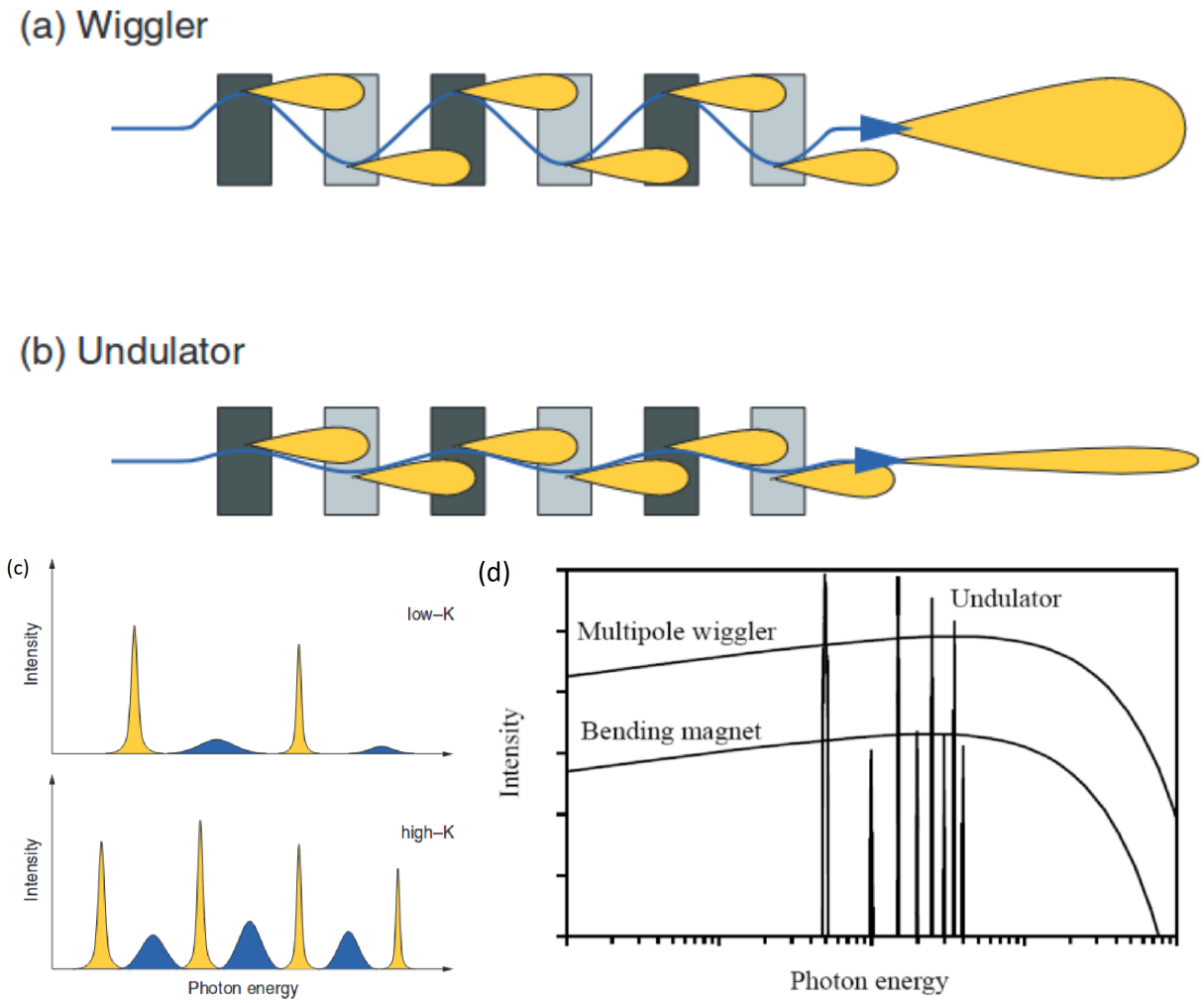

Figure 2.3: Disturbance of forward momentum in the wiggler (a) is larger than in the undulator (b) and therefore the resulting opening angle larger and interference of synchrotron radiation weaker [2]. Insertion device spectrum (c) for low and high K values with harmonic peaks [2]. Overlay of typical undulator, wiggler and bending magnet spectra (d) [11].

2.1.3 Artificial Beams

The properties of synchrotron radiation are highly dependent on those of the electron beam. Electrons in an accelerator or storage ring travel in bunches with each electron varying in position and angle from the beam axis. In an insertion device the superposition of the emissions of all the electrons usually defines the source size unless the electron beam emittance is very small and the source size is defined by the synchrotron radiation's wavelength. This is when one talks about a diffraction limited source.

The aim was to preserve genericness in simulations and avoid modeling a specific undulator or wiggler. This can be achieved using an artificial Gaussian source. For this source standard deviations are defined in the x, y, and z axes for the distribution of rays. Each ray receives also an angle in x and z direction from the y axis based on probability defined by two other preset Gaussians. Finally, a random photon energy is given to each ray based on a range defined by the user.

The source size and angular divergence can be mimicked with this artificial source and be scanned with values found in present day synchrotron facilities.

2.2 Silicon Double Crystal Monochromators

Often synchrotron radiation experiments call for a specific photon energy. This requires that a synchrotron radiation beam be monochromated. Monochromation is the process of separating a narrow band of wavelengths from a multi-spectral radiation source. This can be accomplished by exploiting Bragg's Law

$$n\lambda = 2d\sin\theta_B$$

where λ is the wavelength, d is the interplanar spacing, θ_B is the Bragg angle, i.e. the glancing angle to the diffraction planes, and n is the diffraction order.

At longer target wavelengths it is common to monochromate polychromatic light by means of diffraction gratings or other artificially created periodic structures such as multi-layers. However, when wavelengths approach around 5 Å, current technology is incapable of manufacturing structures small enough. In this case, the periodicity of crystal lattice planes can be exploited. A commonly used material for hard X-ray diffraction is silicon.

Widespread use of silicon in semiconducting devices has allowed industry to develop methods of growing and cutting near perfect crystals. High quality silicon can be considered to have very consistent lattice spacing. However, one must consider the orientation of the lattice. To do this, crystals and notation using Miller indices must be understood.

2.2.1 Crystals and Miller Indices

A crystal is simply an atomic structure that repeats itself identically in all directions of space. Any repetitive unit can be contained in a geometrical region called a unit cell. Each unit cell is defined by the volume constructed from a set of lattice vectors originating from a lattice point. The smallest possible volume they can describe is known as a primitive cell. However, it is often useful to choose lattice vectors forming non-primitive cells (often dubbed "conventional unit cells"). All lattice points in the crystal are given by the vector

$$R_n = n_1\mathbf{a}_1 + n_2\mathbf{a}_2 + n_3\mathbf{a}_3$$

where n is an integer triplet ($n = n_1, n_2, n_3$) and $\mathbf{a}_1,\ \mathbf{a}_2,\ \mathbf{a}_3$ are the lattice vectors. Miller indices, written as h, k, and l, are found by taking the inverse of the lattice vector magnitudes of the 3 points where a plane intersects the lattice axes and finding the lowest common integers that preserve their ratio. The physical lattice plane spacing in any orientation inside a cubic lattice is given by

$$d_{hkl} = \frac{a}{\sqrt{h^2 + k^2 + l^2}}$$

where a is the lattice constant (5.431 Å in silicon). For the case of Si 111, the most common orientation in monochromators ($h = 1,\ k = 1,\ l = 1$), this would make the interplanar spacing equal to 3.136 Å. Silicon monochromators are used for higher order reflections too such as the case of Si 333 with its interplanar spacing of 1.045 Å.

2.2.2 Heat, Deformation and Strain

Absorption of nearly the complete X-ray beam creates an enormous amount of heat in the first crystal. Silicon has the virtue of high heat conductance and with a functioning cooling system is able to dissipate heat well. Despite silicon's low thermal expansion at cryogenic temperatures the crystal still experiences significant warping due to the steep temperature gradients. Of concern, this manifests itself as dips or lumps in the crystal surface near the beam incidence which may significantly alter the reflected beam. Also, strain developed in the crystal lattice in this area may affect reflection due to inconsistencies in interplanar spacing compared to the second undistorted crystal. These two phenomena are investigated in this paper.

2.3 Cooling Systems

In order to dissipate heat deposited in the crystal a suitable cooling system must be installed. Uncountable cooling set-ups have been engineered over the years each carefully designed for its specific application. However, any system can either be classified as "direct" in which a coolant is in direct contact with the object or indirect where an intermediary cooling block is attached. Simulations in this paper involve indirect cooling. Copper cooling blocks sandwich the crystal with good thermal contact on each side. Through holes in the blocks are flushed with 77 K liquid nitrogen. By maintaining the liquid nitrogen temperature and exposing the crystal to a constant beam power a steady state will eventually be reached. A thermal gradient forms between the beam incidence and the liquid nitrogen cooling channels. Sudden changes in the gradient occur at the interfaces between two materials due to their differing thermal conductivities. Even abrupt steps of the temperature may occur at interfaces with heat resistance that can be described by a heat transfer coefficient.

With cryogenic cooling systems it is important to control the temperature of the fluid ensuring that it does not vary by more than a few Kelvin. In the case of liquid nitrogen at 77 K, anything more risks reaching the point of vaporization causing vibrations and removing any cooling effect. There are many factors involved in maintaining such a strict temperature range including the refrigeration systems for the coolant, precision pumps, as well as the design of thermal contact to the crystal. However, these aspects of the system are designed apart from detailed simulations including shifting Bragg angle due to crystal strains.

Controlling the flow rate is more or less a matter of changing a variable or two in the simulation, however, improving heat conduction is much more involved. In order to enhance heat transfer lateral to the direction of flow turbulence may be induced. Turbulence is an erratic state of fluid flow involving sudden changes of pressure and velocity over time at essentially random points throughout a body. This study uses COMSOL for fluid flow modeling.

3 Ray Tracing and Finite Element Analysis

The bulk of the study is performed using combined ray tracing and finite element analysis. Once each method has been prepared individually a highly automated framework called MASH runs simulations combining the two. MASH provides its own analysis and visualization tools but also raw output data for external evaluation.

3.1 Ray Tracing using SHADOW3

Ray tracing is a technique used to predict the propagation of radiation as it enters and exits various media. Sundry interaction phenomena can be ignored or considered depending on the needs and capabilities of the code including, for example, absorption, reflection and diffraction. In any case, often these interactions are so numerous and complex that one turns to a well established computer code to perform the simulations to ensure it has been tested many times before. This study uses SHADOW3 [12], a popular and powerful Fortran code under development since the late 1970s.

The code is well equipped for the simulation. To begin, synchrotron light sources can be produced in the forms of generic artificial sources, bending magnets, undulators or wigglers. From there, many common beamline components can be readily inserted into the ray paths. In addition distortions of the optical elements, e.g. due to heat loads, can be considered.

Importantly, the capabilities of modeling crystal monochromators is well developed. SHADOW3 is able to model diffraction from crystals of varying lattice orientation, i.e. any combinations of Miller indices, as well as surface imperfections such as dips or protrusions. Surface imperfections can be implemented natively by a map of surface deformation provided by the user to SHADOW3. This deformation map can be created by modeling thermal expansion and elastic deformation due to X-ray absorption in external programs such as COMSOL, a technique described in Section 3.2. Surface reconstruction uses a spline interpolation to avoid creation of grating like structures that can often be found in linear interpolations.

Where SHADOW3 falls short, however, is the ability to calculate the diffractive effects of varying lattice spacing due to strain in the crystal. In order to include these effects significant modifications would have to be made to an already complex code. For non-developers, this would be an enormous task not only initially, but to maintain over new editions to the code. Preferable is to discover a way to implement these effects in the code in an encapsulated manner so that future changes to SHADOW3 code do not interfere.

In Section 4.1 the effects of uniform strain gradients along the surface normal of the crystal are considered. It is found that the effect on diffraction of a lattice constant varying over depth under less than extreme conditions is negligible in Si 111. There is, however, potential for gradients to play a role in higher order reflections such as Si 333 under high power loads. Since this study will be considering only medium power beams the lattice constant at any point in the plane of the crystal surface can be considered constant with depth.

A simple trick to avoid implementing a varying lattice constant was developed and implemented by Peter Sondhauss and described in the immediately following text. Bragg's Law is given as

$$n\lambda = 2d \sin\theta_B$$

where λ is a photon's wavelength, d the crystal's interplanar spacing, θ_B is the Bragg angle, and n a positive integer representing possible reflection orders. By rewriting the expression as $\lambda/d = (2/n)\sin\theta_B$ it can be noticed any change in interplanar spacing, $d_0 \to d$, can be interpreted instead as a change in wavelength, $\lambda \to \lambda'$, so long as the ratio $\lambda/d = \lambda'/d_0$ holds. Therefore instead of entering a new lattice spacing at every point an artificial wavelength, $\lambda' = \lambda d_0/d$, can be used during diffraction calculation. The trick begins as ray tracing reaches the point of incidence on the crystal and an output file of the positions of rays and their properties is created. This file is then compared to a map of the strain at respective points and wavelengths are shifted accordingly. Reflection then commences with the new wavelengths and another file for the output is created. This file is then parsed and the wavelength transformation is reversed. The additional computational costs of the trick are quite minimal and surely are merited by the avoidance of the time requirements for alterations concerning the varying lattice spacing to the SHADOW3 source code.

Two considerations must be made when implementing this wavelength shift. First, a change in wavelength will result in a different angle of refraction. Refraction is a small to start with and will be minuscule

considering the small wavelength shift. Second, the absorption properties of silicon differ based upon wavelength. Fortunately, only unrealistically large changes in lattice constant will allow these effects to be noticed. However, the latter effect can be significant when a wavelength is near an absorption edge. Here even small changes in wavelength can have a dramatic effect since the change in absorption is so abrupt. Fortunately, neither of these problems are an issue within the parameters of this study.

3.2 Finite Element Analysis using COMSOL Multiphysics

In order to determine surface distortions and lattice strain due to thermal expansion or contraction from X-ray absorption thermoelastic simulations were performed. However, to solve these problems analytically complex boundary value problems encompassing many highly coupled physical equations must be solved. With anything but the most basic geometries this is a monumental feat. In modern engineering, this is most often left to a Finite Element Analysis computer program. Finite Element Analysis (FEA) is a mathematical technique that numerically approximations solutions for equations on subsets of a given domain. Combined, they solve the entire geometry.

FEA is a vast and well developed subject. As interesting as it is to learn, many users only retain basic knowledge of the method and rely on implementation and optimization of its techniques through pre-developed software. However, some software allows advanced users to fine tweak physical equations and mathematical methods to their liking. A popular and powerful program that allows just that is COMSOL Multiphysics [13]. It is the FEA software of choice for this study.

COMSOL usage is mainly through a graphical interface though it can alternatively be controlled programmatically via MATLAB [14]. The general workflow proceeds as follows.

1. A geometry is built using CAD (computer-aided design) to represent the physical object being modeled.

2. Each part of the geometry is given a specific material. The material definition includes physical properties needed for the simulation such as a coefficient of thermal expansion or a Young's modulus. In some cases these values will need to be found in literature and then added. In others, the values must be redefined as a function to include, say, temperature dependence.

3. The next step is to add boundary conditions. For example, heat resistance by a laminar layer of a flow of liquid nitrogen in a pipe, heat exchange between copper and silicon in thermal contact or stresses in a system under a clamping force. One can also add "multiphysics", that is, mathematical coupling between any two physical processes. An example is thermal stress where the temperature induced expansion of a material results in stress.

4. A mesh is added to the geometry. The mesh creates the "finite elements" in Finite Element Analysis. Often these elements are 3 dimensional tetrahedrons tessellating a volume but can also be a variety of shapes depending on what is being modeled. Meshing is a complicated topic which fortunately is highly automated in COMSOL. The user can redefine the mesh based on knowledge of the physical processes and drawing on prior experience and references to successful simulations. For example, one may want to implement what is called a "swept mesh" in regions of fluid flow to improve computation or a much finer mesh in areas where a precise power distribution is entering an object to improve accuracy. Often a poorly defined mesh can prevent a solution from being found or deceptively provide one with poor accuracy.

5. The next step is to define a study. The study is a set of options telling COMSOL what to solve and how to solve it. One may want find a solution while neglecting one physical process. Perhaps a "parameter sweep" is required and the program should solve the equations for 10 different fluid flow speeds. It could be that the user seeks a time dependent solution instead of a steady-state one. Once the study is prepared the user can execute it and solving will begin. Studies can take anywhere from less than a minute to hours, depending on the complexity and computing resources.

6. COMSOL also has a results section. This section provides plotting and post solution calculations such as max, min, average or integrated values of a variable within a given domain. Results can also be exported for external analysis.

Among the results of a COMSOL thermoelastic simulation are deformation and strain maps on the crystal's reflecting surface. These can be used as input to the earlier described ray tracing.

3.3 Combing Ray Tracing and FEA using MASH

Often FEA and ray tracing simulations need to run repeatedly and in conjunction using many different input parameters. For example, a monochromator may want to be studied under different Bragg angles and beam conditions. In order to avoid monotonous human interaction these scans are left to automation via the software MASH.

MASH (Macros for the Automation of SHadow) is a framework written by Peter Sondhauss that integrates COMSOL FEA and SHADOW3 ray tracing [15]. The program is run remotely via a web interface which provides the user with a plethora of options for the performance of simulations. Notably, it includes templates for common light sources, optics and FEA models. It also has its own data visualization as well as the ability to export raw data. Importantly, it is capable of scanning various properties of a beam, such as varying source size or total power. An advantage of MASH is that it is flexible in its design and readily accepts new COMSOL models into its calculations. Details of the models and parameters used during simulations are given in Section 4.

The main task of MASH is to perform scans over a range of energies. Each energy defines the settings of the optics, namely the monochromator, and the number from which values such as bandwidth are calculated. These energy scans are repeated over a range of cases. Cases are defined by varying any parameters other than photon target energy in the simulation. An example would be Case 1 having a monochromator 20 meters from a source while for Case 2 it's 40 meters. The number of cases in a simulation has to stay under the set limit of 40.

4 Models and Simulations

4.1 Crystal with a Uniform Strain Gradient

As described in works by Chukhovskii [16] and Taupin [17], under certain conditions a strain gradient perpendicular to a crystal surface can have a dramatic effect on reflectivity. An analysis was made in order to deem the importance of this strain gradient. If insignificant, complexity of the simulations would be drastically reduced as major modifications to the existing SHADOW3 ray tracing code could be avoided. Computer code for calculating crystal reflectivity within the framework of the dynamical theory of X-ray diffraction was written, validated and provided by Peter Sondhauss as described in Reference [18]. Plotting was performed by the programming language Python [19]. It was determined that a uniform strain gradient in Si 111 has an insignificant effect on crystal reflectivity and can therefore be ignored here. Si 333 was noticed to be affected strongly by a strain gradient at only moderately high temperatures. Although, the temperatures are outside the range of what is studied and therefore are ignored. See Section 5.1 for further description.

4.2 FEA Models

3 models were successively built in COMSOL each with increasing complexity. The first model was simply a block of silicon with a defined constant temperature on two opposite sides. The second is a model with copper cooling blocks and fluid flow. Finally, the third is a detailed model of the monochromator found identically at NanoMAX and BioMAX. Parameters used in simulations are found in Appendix B.

4.2.1 Silicon-Only Model

The first model is quite rudimentary but its simplicity and low computational costs are useful for preliminary testing. It consists of a $20 \times 40 \times 50$ mm^3 block of pure silicon crystal with beam incidence on the top surface and set temperatures on two of its sides. The crystal is kinematically mounted meaning it is fixed in place without limiting the ability to expand in all three directions. The model also features a section of exceptionally fine mesh where the beam is incident. It is fine enough to outline the entire beam profile and has a gradual increase in size until reaching the normal mesh size of the rest of the silicon body. This fine mesh is important in order to be sensitive to the shape of the power footprint. The meshed silicon block and close-up image of the mesh adjustment are seen in Figure 4.1.

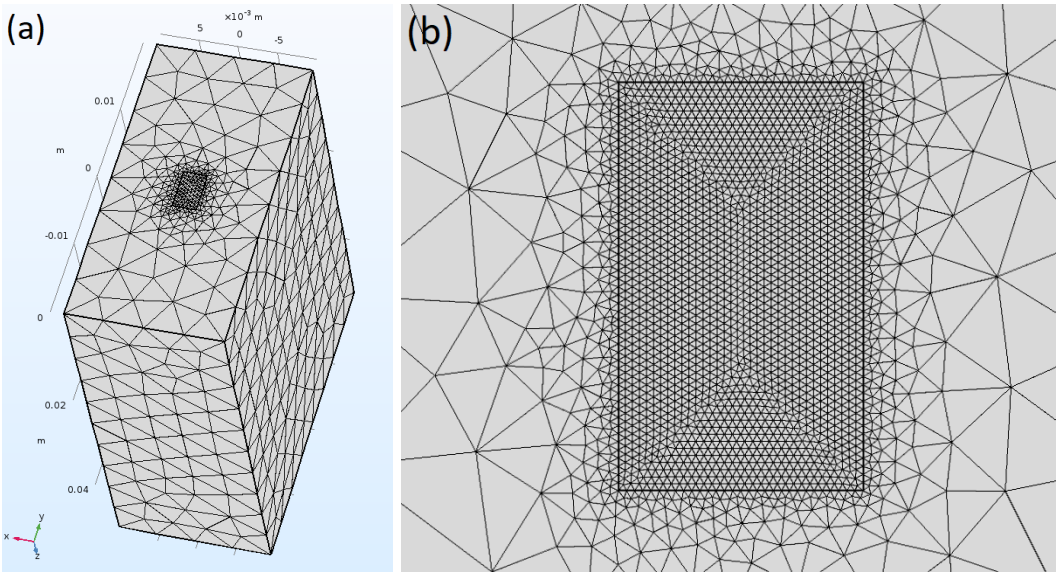

Figure 4.1: (a) COMSOL geometry of a $20 \times 40 \times 50$ mm^3 block of silicon (b) The refined mesh area is 5×3 mm^2 and centered at the origin of the COMSOL coordinate system.

A power distribution from an undulator source was created in SHADOW3 and was used in all preliminary studies, i.e. all studies outside those performed in MASH in which inputs to FEA models are explicitly stated. It is plotted in Figure 4.2. The total power provided to the silicon from this source was a steady 130 W. COMSOL does not provide a temperature dependent template for silicon in its materials library. Therefore one must derive and insert functions of temperature for the secant coefficient of thermal expansion, α, and the thermal conductivity, κ. This was done using techniques developed in Reference [15].

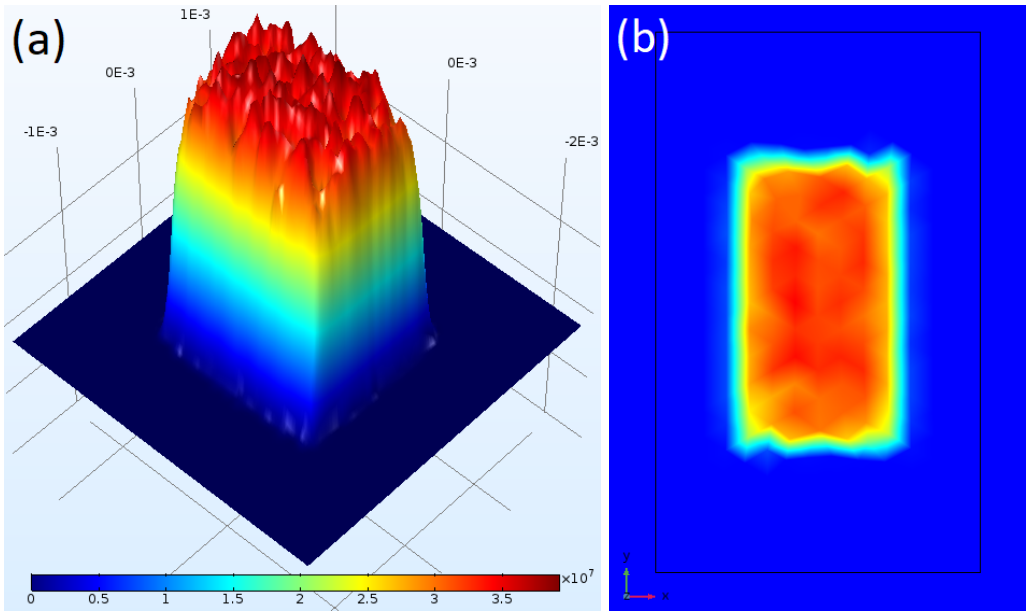

Figure 4.2: (a) Plot of intensity in W/m^2 as a function x and y (b) Application of the function as a heat load within the outlined fine mesh area. The total power accepted by the silicon block is 130 W.

This model was used to perform several so-called "parameter sweeps" in COMSOL. The value of the cooling temperature on the sides of the silicon was set as a variable and simulations were run with it set to a range of values. The results provided extrema of temperature, stress and strain gradient in the silicon within the area of beam incidence. These numbers were ran through the numerical model described in Section 4.1 and the results plotted in Section 5.1. Further discussion is found in the results section.

4.2.2 Basic Fluid Cooled Model

The second model adds copper cooling blocks flushed with liquid nitrogen and is seen in Figure 4.3. It is slightly more complex as it necessitates the modeling of turbulent fluid flow. This model is purposely generic, serving as a stepping stone towards the model of the NanoMAX and BioMAX monochromator.

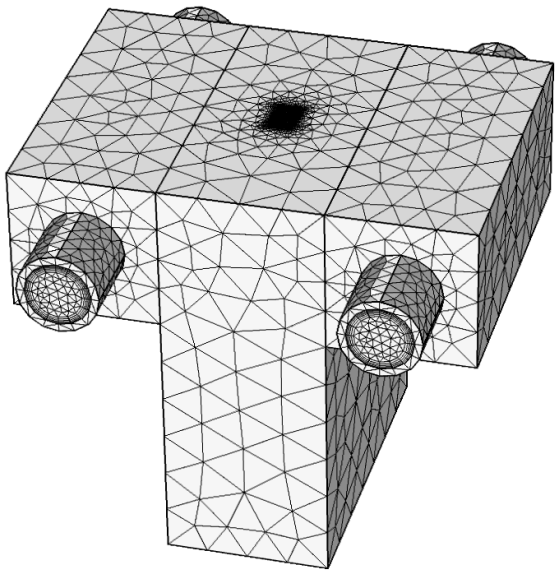

Figure 4.3: A model with the addition of copper cooling blocks to the silicon crystal. A swept mesh is applied to the fluid flow regions seen within the protruding copper piping.

The importance of adding turbulent fluid flow to the model is to get a realistic idea of the thermal resistance at the pipe periphery and hence the temperature and stress fields. Those fields determine the strain in the crystal and as a result the reflected beam profile and spectrum. One must note that the side mounted cooling blocks threaten to add additional stresses as they expand and contract inharmoniously with the silicon. Under certain circumstances this may influence the strain near the beam incidence. Modeling this effect, however, is not the goal at this stage and stresses due to mismatch in thermal expansion are eliminated by adding damping forces at the materials' interface in the simulation.

The model used in COMSOL for simulating the fluid flow is the $k-\epsilon$ RANS model with default parameters. By adjusting the fluid flow rate a suitable speed is found that prevents the 77 K nitrogen from heating by more than a few kelvins. This allows the temperature dependent properties of nitrogen to be disregarded, especially of those at or near the boiling point. The fluid flow can be tweaked further to find a heat distribution that minimizes strain in the silicon crystal.

4.2.3 NanoMAX and BioMAX Monochromator Model

The third model is slightly more complex. It is a simplified replica of a monochromator found in the beamline optics of NanoMAX and BioMAX at MAX IV and is seen in Figure 4.4. The monochromators were built by the same manufacturer and for the purposes of this simulation can be considered identical. Between each block and the crystal an indium foil of 50 μm was added.

It is a challenge to introduce accurate stresses induced by mounting of the cooling system. The silicon is sandwiched between two oversized copper blocks and held in place by a clamping force. The kinematic mounting shifting from the silicon itself to the larger copper cooling block may affect stress. Differing coefficients of thermal expansion between copper and silicon can lead to stresses exceeding that of the temperature gradient at the beam incidence. Numerous assumptions can be made in which simulations are bound to become labyrinthine. Therefore, it is suitable for an initial study of previously uninvestigated effects to assume the manufacturer has accounted for such stresses and taken on the task of minimizing them. However, in the future, it will be of interest to study whether there are effects on the beam that can be attributed to such stresses and in what way they can be modeled.

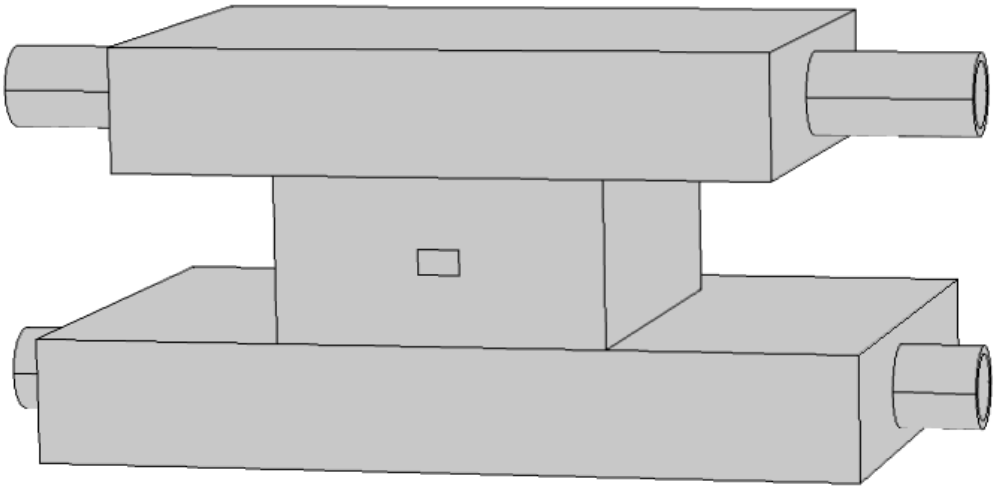

Figure 4.4: A model of the first crystal of the NanoMAX and BioMAX monochromator

4.3 Simulation Step by Step

Simulations in this study require the two synchronized methods ray tracing and FEA as described above. The general flow of the simulation is presented in Figure 4.5 and explained in the immediately following text. Note that all steps will be explained, however in practice any of the lower 3 steps in the figure can be skipped depending on the goal of a simulation. The steps break down as follows.

1. The first step in these simulations is to employ a ray tracing code, in this case SHADOW3, to simulate the beam source. The source was first modeled as an artificial geometric source with control over all properties such as source size, divergence, and bandwidth.

2. In this step one can model components in the front end and optics section of the beamline. In basic simulations there are no components between the source and the first crystal.

3. The ray tracing code then creates data for the beam incidence on the first crystal including angle of incidence, power and wavelength of the incoming rays. Intensity data can be fed into an FEA program such as COMSOL.

4. If one wishes to model the effects of heat on the crystal the data from the beam incidence can be sent as a power distribution to an FEA program. In the program the power is set as a heat flux boundary condition. The FEA model produces as an output a map of the strain and physical deformation on the crystal surface.

5. Diffraction in the first crystal is modeled by the ray tracing code and, if provided, considers strain and deformation. Rays reflected from the first crystal are then to be reflected from the second. For the second crystal, simulating thermally induced imperfections are not necessary due to the majority of the power being deposited in the first. The second crystal absorbs a very small amount of power.

6. One may want to simulate additional optics after the monochromator. However, in this study the beam is only examined directly after the second crystal.

7. The output of the ray tracing is handled by MASH. It organizes the data in plots, reports and detailed text files. The text files provide data needed for external data analysis, such as by using Python and its various packages.

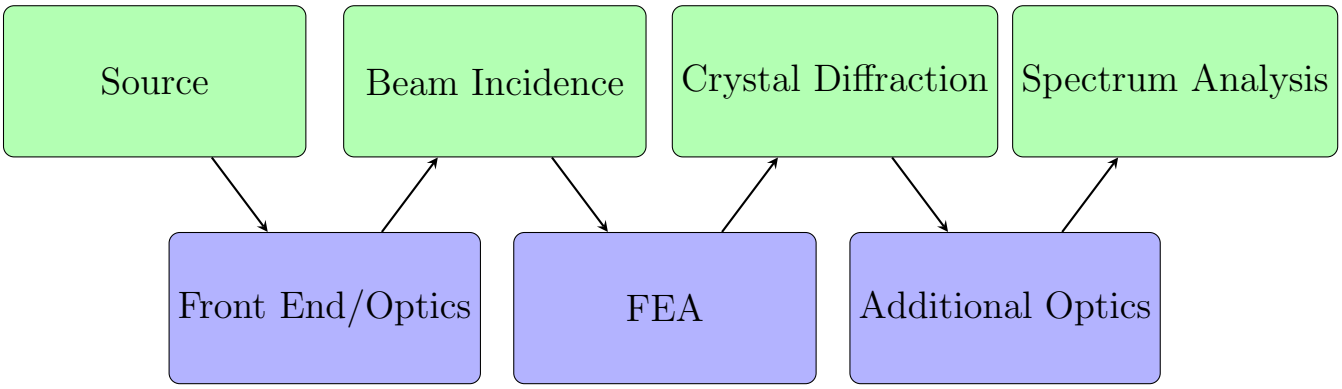

Figure 4.5: A flowchart describing the simulation methods used in this study. The top row (green) are the essential parts of the simulation while the second row (purple) are optional additions providing for the study of various effects.

4.4 Parameter Scans

In order to understand the fundamental relation of the monochromator performance with certain parameters, parameter scans were performed in MASH. Due to its higher sensitivity to strain, scans using the 333 reflection of silicon were most interesting with which to begin. The simplest model was a good starting point as it allows the effects of varying parameters like source size and source power to be seen more plainly. The silicon-only FEA simulation was used along with an artificial Gaussian beam source emerging from a position 20 meters from a horizontally deflecting double crystal monochromator. So-called "continuation planes", i.e. imaginary planes used for probing beam parameters, were set up after each crystal. Components and photon path lengths separating them can be seen in Figure 4.6. Using this model, energy scans proceeded as follows.

1. This scan was performed with photon energies ranging from 6 to 35 keV in 1 keV intervals. A source size of $50 \times 5 \times 5$ μm^3, for $(x,\ y,\ z)$, was used with a Gaussian spatial and angular distribution and a total power of 150 W. The scans were performed under four considerations: no strain or deformation, deformation with no strain, strain with no deformation, and finally with both strain and deformation.

2. The same scan was repeated this time but with varying the value of the total power through levels 50 to 200 W at intervals of 50 W.

3. The first scan was repeated again though varying the source size. The values for the source size in the horizontal and vertical (i.e. $x,\ z$) were set as, in microns, (0,0), (25, 2.5), (50, 5), (75, 7.5), and (100, 10).

4. Due to the spreading of the beam the distance between the source and the first crystal will have an effect on the incident power per unit area while keeping the total power and beam divergence constant. Therefore, to adjust this intensity in a scan a simple change in distance will suffice. Distance between the source and first element were varied as 20, 40, 60, 80 meters with the remaining parameters being identical to the first scan.

5. The divergence of the beam will have a strong effect on reflection off any optical component and is therefore included in its own scan. The scan was run with values of divergence, $(x,\ z)$ in μrad, set at (25,25), (50,50), (75,75), and (100,100).

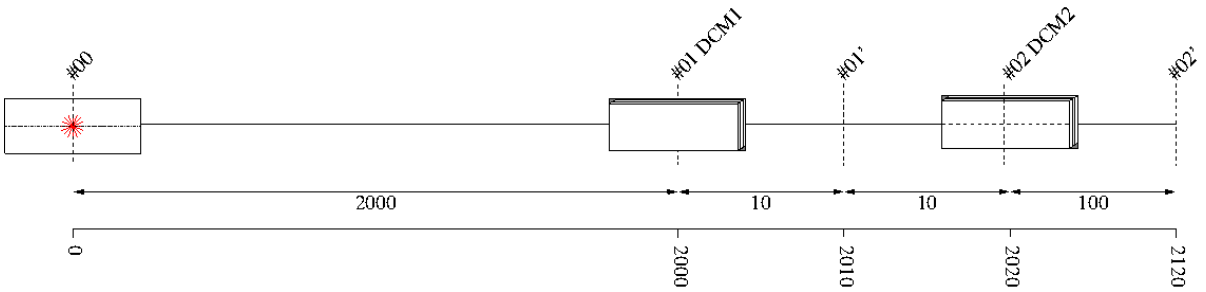

Figure 4.6: Scheme produced by MASH showing the set up used during parameter scans 1-5 [12]. The vertically dashed lines are "continuation planes" which are imaginary surfaces used by ray tracing code to take a snapshot of beam parameters at the point which they cross. Distance units given in cm.

4.5 Second Crystal Compensation

An argument can be made that attenuation due to strain may be compensated for by adjusting the angle of the second crystal relative to the first. For the most intense part of the beam strain in the first crystal will be highest and therefore also the difference between the lattice spacing of the two crystals. One could adjust the second crystal to allow for greater reflection of this intense portion at the sacrifice of less intense parts. Although, this optimization has to be repeated every time the monochromator is tuned to a different photon energy. This is certainly feasible at beamlines working at more or less fixed photon energies. For a fast scanning monochromator this is most likely impractical.

5 Results and Discussion

The first result was concerning the effects of a uniform strain gradient in Si 111 and Si 333. It is described in Section 5.1. By concluding that it can be disregarded the complexity of the remaining studies was drastically reduced. Secondly, the crystal surface deformation was analyzed. This is described in Section 5.2. Indeed, it can change the angle of rays considerably and should be regarded. After this, parameter scans in MASH including the effects of a two dimensional strain field across the surface of the first crystal (without strain variation into the crystal bulk) are described in Section 5.3.

5.1 Uniform Strain Gradient in Si 111 and Si 333

To determine the approximate levels of strain gradient present in a crystal under typical operating conditions the simple silicon-only model was used in COMSOL. Side cooling temperatures were set at intervals with each one producing a solution for the extremum of temperature, von Mises stress, deformation and strain gradient found in the crystal. The numerical methods described in Section 4.1 were used with a wavelength value of 1 Å to generate the plots describing reflections in a Si 111 crystal in Figure 5.1. From the plots one can notice that effects of the strain gradient do not clearly develop until around a cooling temperature of 160 K, Figure 5.1d. Near the beam the maximum temperature in the silicon is about 305 K, which is completely beyond an acceptable operating temperature. Even then the effect is minimal. With this data it is concluded that the effects of a uniform strain gradient on the Si 111 reflection need not be considered.

However, higher order reflections, say in Si 333, tell a somewhat different story. The same numerical methods were used to generate plots in Figure 5.2. In these plots one can see the effect of strain at every temperature. Note that even around a reasonable operating temperature of 130 K, Figure 5.2e, the effects are clearly visible. However, when averaging out these oscillations the curve is not considerably deviant. Reaching higher temperatures such as the case in Figure 5.2f, at a maximum temperature of about 145 K, the curve drifts more dramatically. These temperatures are likely not to be reached except perhaps in the case of receipt from a high powered wiggler. Due to the complexity of modifying the SHADOW3 code and the time limits of the study, along with its concern towards the lower operating temperatures, these high temperature conditions are not studied.

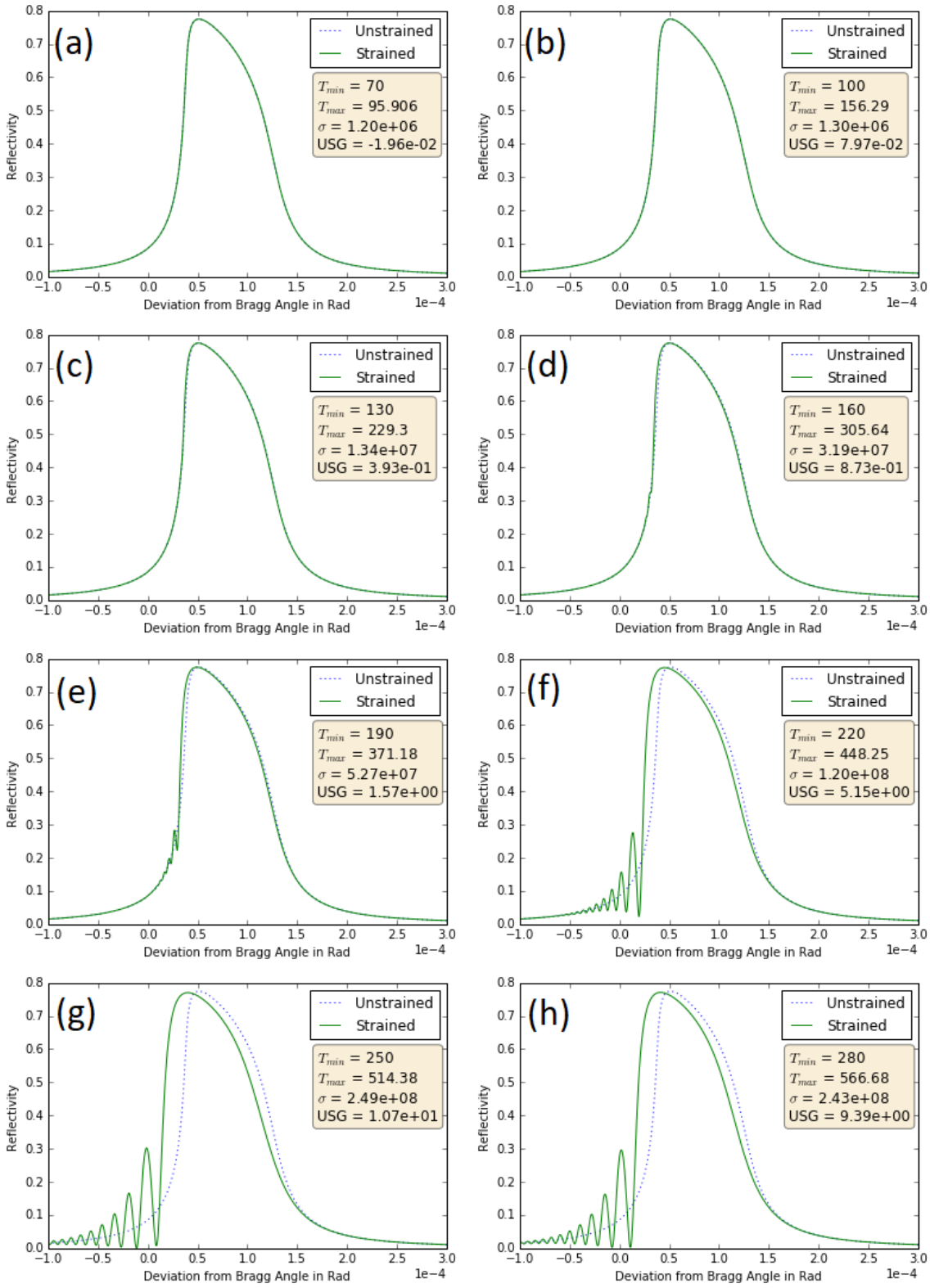

Figure 5.1: Calculated Si 111 rocking curves with a uniform strain gradient (USG) of (a) -0.0196, (b) 0.0797, (c) 0.393, (d) 0.873, (e) 1.57, (f) 5.15, (g) 10.7, and (h) 9.39. Temperature (T_{min}, T_{max}) is given in kelvins and von Mises stress (σ) in pascals.

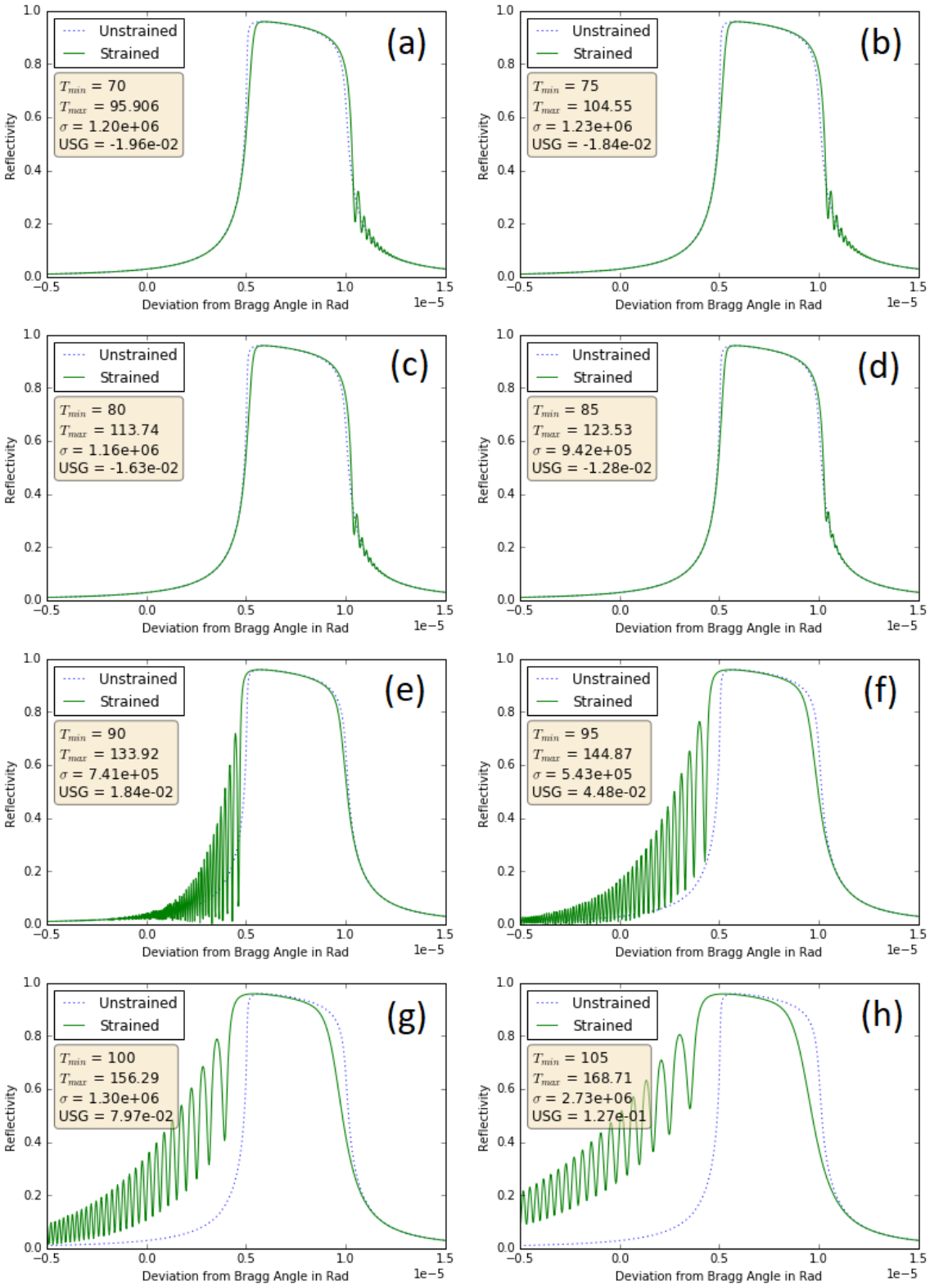

Figure 5.2: Calculated Si 333 rocking curves with a uniform strain gradient (USG) of (a) -0.0196, (b) -0.0184, (c) -0.0163, (d) -0.0128, (e) 0.0184, (f) 0.0448, (g) 0.0797, and (h) 0.127. Temperature (T_{min}, T_{max}) is given in kelvins and von Mises stress (σ) in pascals.

5.2 Crystal Surface Deformation

Deformation of the crystal surface affects reflection by changing the incident and reflection angle due to deformation altering the slope. The altered slope in turn changes reflectivity as interference conditions change. Conveniently, the MASH framework and SHADOW3 consider the effects of surface deformation and include it in their calculations. Therefore, manual analysis is only necessary in order for the reader to understand qualitatively the effect of deformation on the output.

Briefly, surface distortion calculated in the silicon-only model is presented. One can see in Figure 5.3 charts of the z displacement as a function of y (beam travel direction). The position of x is set to 0 so that the data is provided by a line crossing the center of beam incidence. Temperature is also plotted and is the curve looking nearly identical in the different plots apart from amplitude.

An interesting observation is that at the temperature with zero thermal expansion the deformation curve inverts itself, and emerges from its trough, forming a peaked structure. The most important parameter however is the slope of this deformation, as it affects the incidence and reflected angle of the rays. The derivative of the z deformation with respect to y is calculated and presented in Figure 5.4. In the reasonable case of 133 K maximum temperature, Figure 5.4a, the slope error is about 8 μrad. This 8 μrad is of the order of the rocking curve widths in Figure 5.2 and therefore significant changes in throughput can be expected. It is quite crucial then to model the deformation accurately and include it in ray tracing simulations.

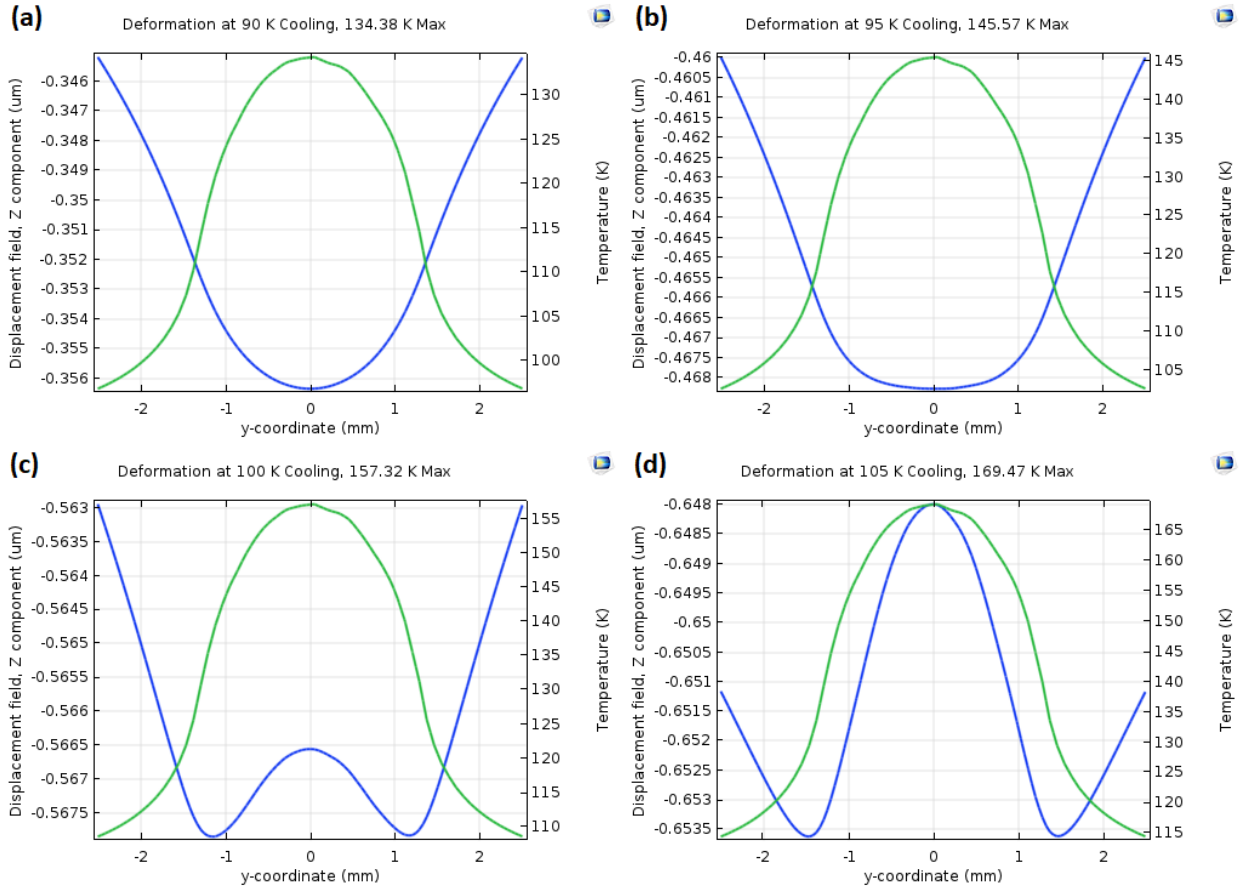

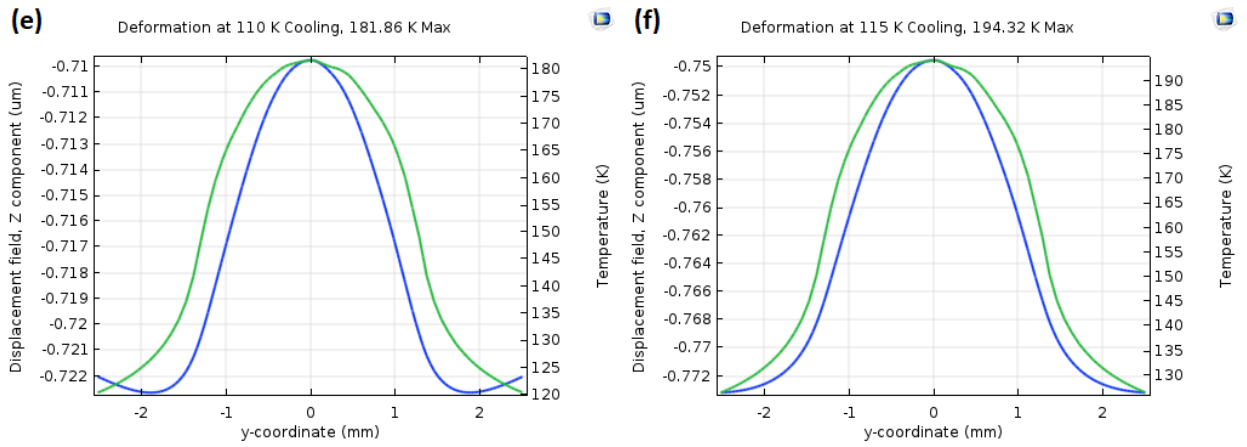

Figure 5.3: Deformation of the crystal surface near beam incidence. Temperature is shown as the green curve while deformation the blue. As the maximum temperature rises from (a) 133 K to (b) 144 K, (c) 156 K, (d) 168 K, (e) 180 K, and (f) 192 K the dip inverts itself

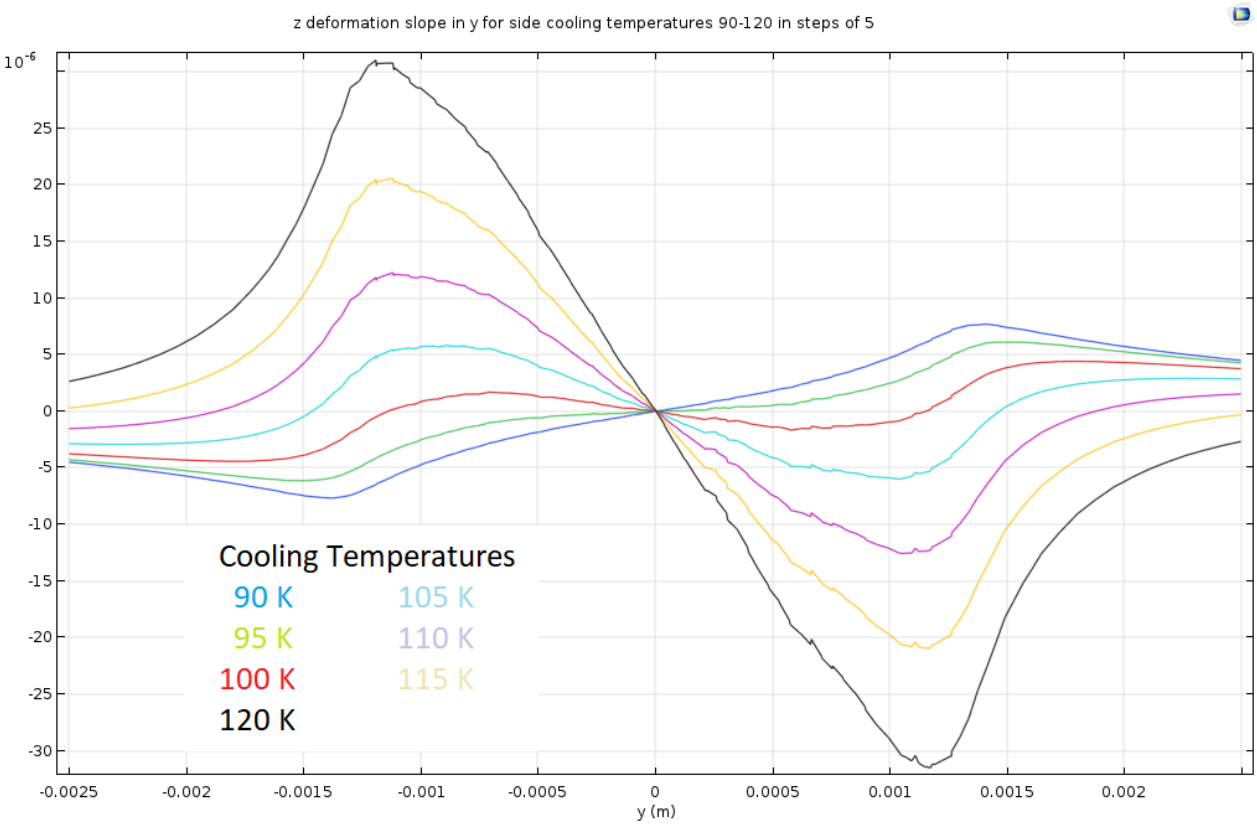

Figure 5.4: Slope of the z deformation on the vertical axis in meridional direction (y) near the beam incidence

5.3 Si 111 with Two Dimensional Strain Field

It has been concluded that a uniform strain gradient in Si 111 has no considerable effect. But what about strain constant in depth though varying across the crystal surface? Does this affect the overall reflectivity of the combined crystals? Does including the effect of deformation enhance or diminish the effects of the strain? To find out, scans over the energies 6 to 35 keV were performed in MASH with and without strain included and then again including surface deformation as described in Scan 1 in Section 4.4. The group of

scans receive the following treatment.

1. A chart of photon flux reflected off the second crystal as a function of scanned energy for each case is included. The chart has a line with and without strain as well as one for the relative error.

2. Bandwidth of the monochromating system is also plotted for the energies in the scan. That is, the standard deviation of the reflected spectral distribution divided by the central energy defined by the monochromator setting.

3. Charts of the spectral flux around the central photon energy in the energy scan are provided.

A look is taken at the total photon flux per energy setting found at the continuation plane after the second crystal. Figure 5.5 charts 2 times Si 111 reflected flux ignoring and including surface deformation. In both cases the strained crystal curve follows closely that of the unstrained and at no energy does the relative difference between them reach above 3%.

Figure 5.6 shows the monochromator bandwidths (standard deviation) as a function of set photon energy ignoring deformation or considering it. They are nearly the same between the two cases, this time with a deviation below 1%.

Reflection curves in Figures 5.7 (no deformation) and 5.8 (with deformation) tell a similar story; they are nearly identical between strained and unstrained cases.

The conclusion is that the effects of strain in this model are negligible. However, it is still worth investigating Si 111 monochromators in more realistic setups such as the NanoMAX and BioMAX models.

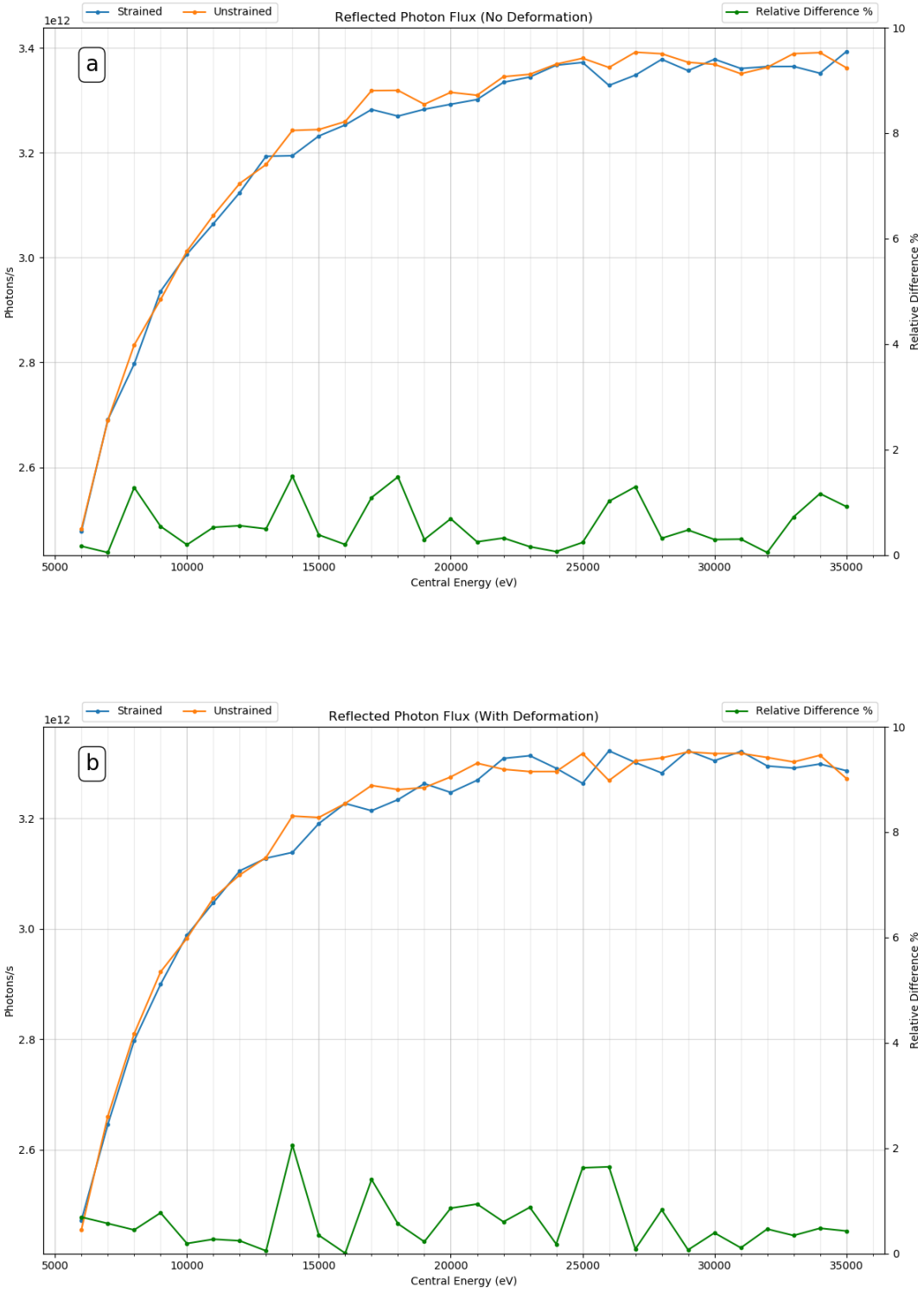

Figure 5.5: Photon flux leaving the Si 111 monochromator with strained and non-strained first crystal (a) ignoring surface deformation, (b) including deformation

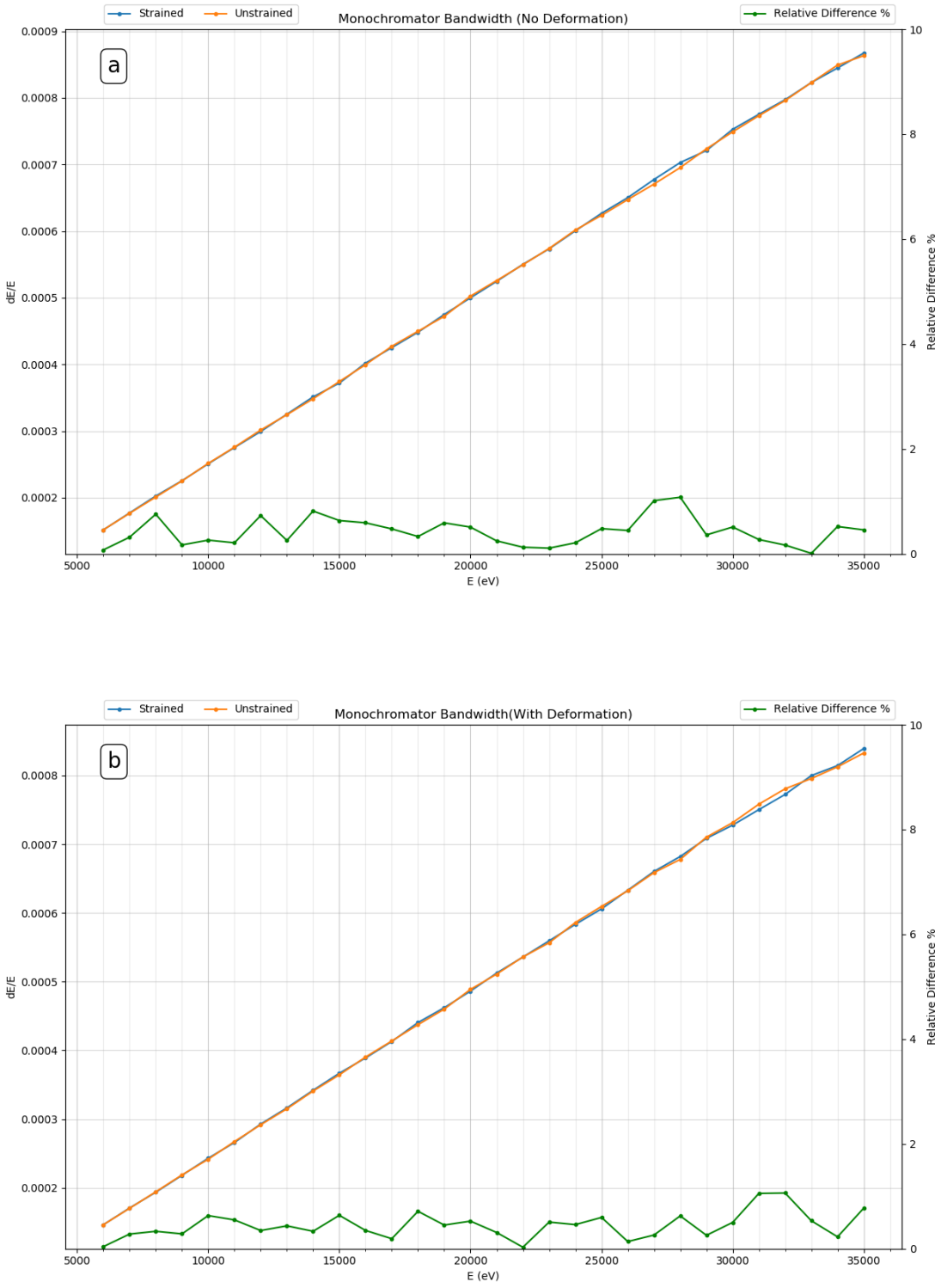

Figure 5.6: Si 111 Monochromator bandwidth (dE/E, standard deviation) with strained and non-strained first crystal (a) ignoring surface deformation, (b) including deformation

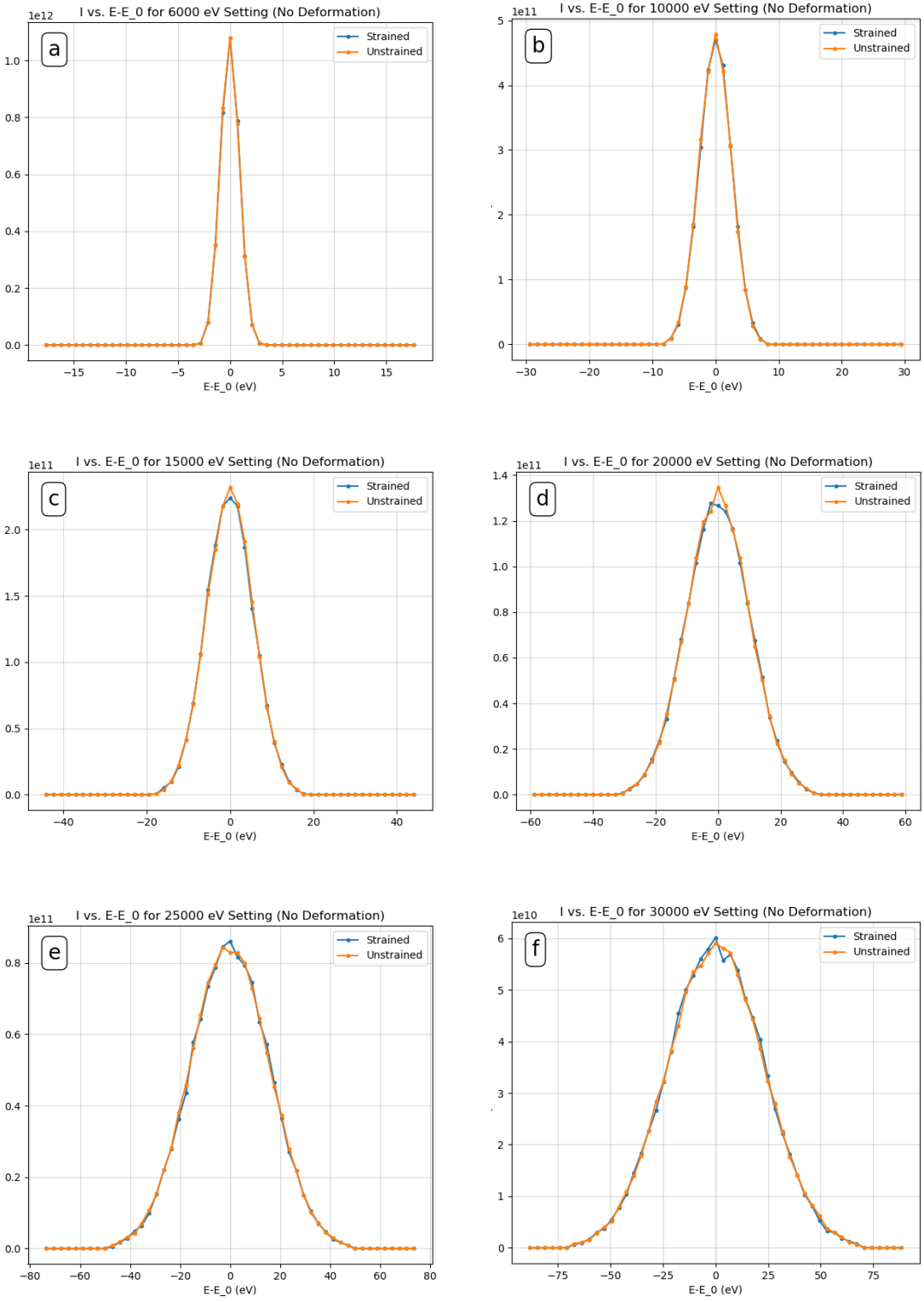

Figure 5.7: Two times Si 111 reflection curves with and without strain at (a) 6 keV, (b) 10 keV, (c) 15 keV, (d) 20 keV, (e) 25 keV, and (f) 30 keV photon energy settings. The y axis is given as photons per second per eV. Surface deformation is not considered.

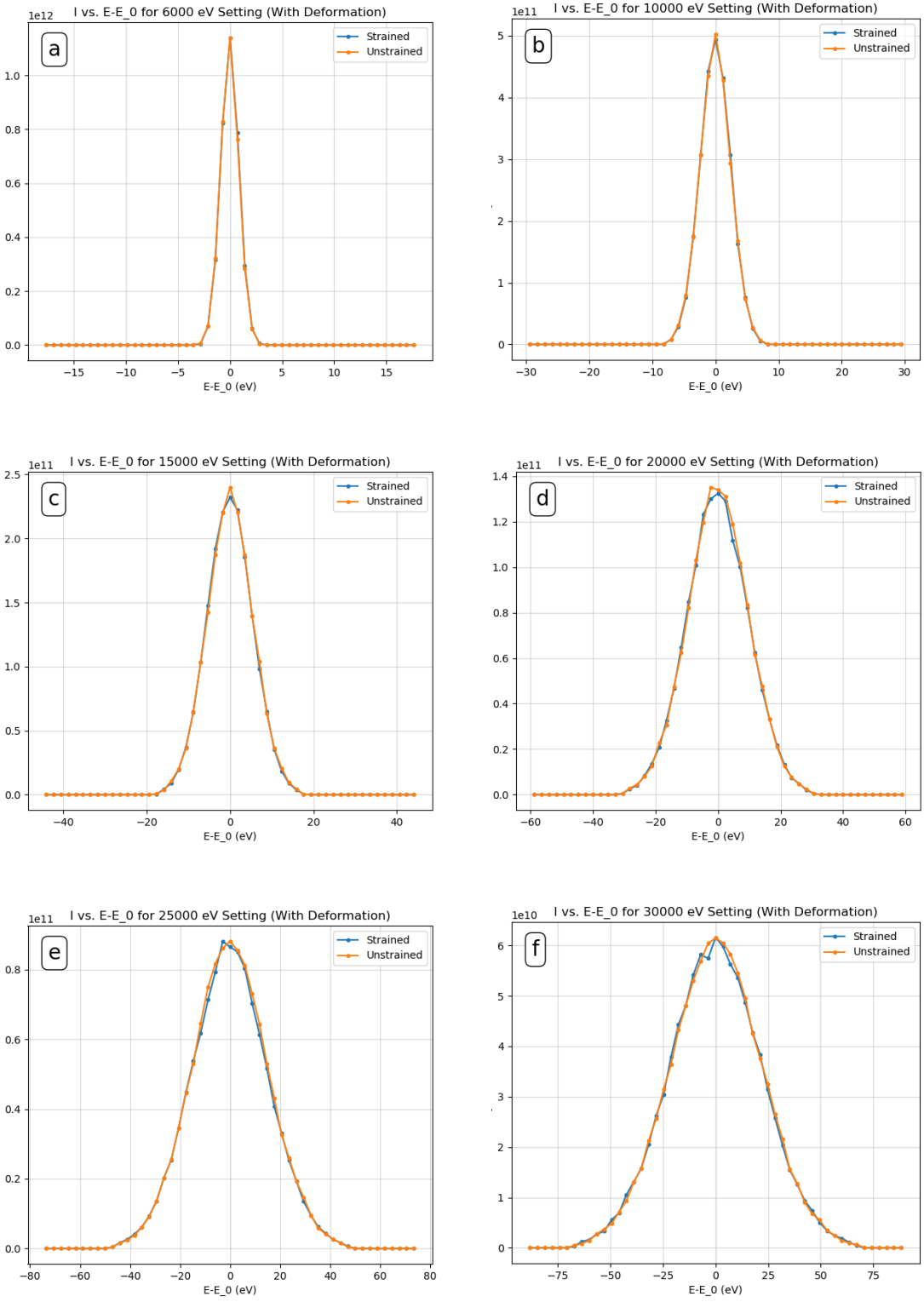

Figure 5.8: Two times Si 111 reflection curves with and without strain at (a) 6 keV, (b) 10 keV, (c) 15 keV, (d) 20 keV, (e) 25 keV, and (f) 30 keV photon energy settings. The y axis is given as photons per second per eV. Surface deformation is considered.

5.4 Si 333 with Two Dimensional Strain Field

The simulations in Section 5.3 were performed again, differing only the Miller indices, now 333. Unlike for Si 111 the results with and without strain were drastically dissimilar. In Figure 5.9a it is seen that in the case without deformation, the monochromator with strained first crystal has a throughput about 30-60% below the unstrained case. Throughput increases for both cases towards higher photon energy and the relative difference between them decreases. Figure 5.9b shows the effect of strain including deformation. Surprisingly, the disparity between the strained and unstrained case is quelled by the deformation. It begins at 60% decreasing to below 20% near 25 keV. This raises the interesting question: under which conditions does deformation increase throughput in strained crystals?

Monochromator bandwidths follow a similar upward trend as in Si 111. However, the relative difference between strained and unstrained crystals is increased as seen in Figure 5.10. Again, this difference decreases when considering deformation (Figure 5.10a), though only by a few percentage points.

Figure 5.11 shows reflection curves at the various energy settings with no deformation. One clearly sees the attenuation in the strained case. In Figure 5.12 one notices that strain in the deformed crystal shifts the curve towards lower energies. Figure 5.12f, i.e. the 30 keV case, shows the peak energy shifted by 2 to 3 eV.

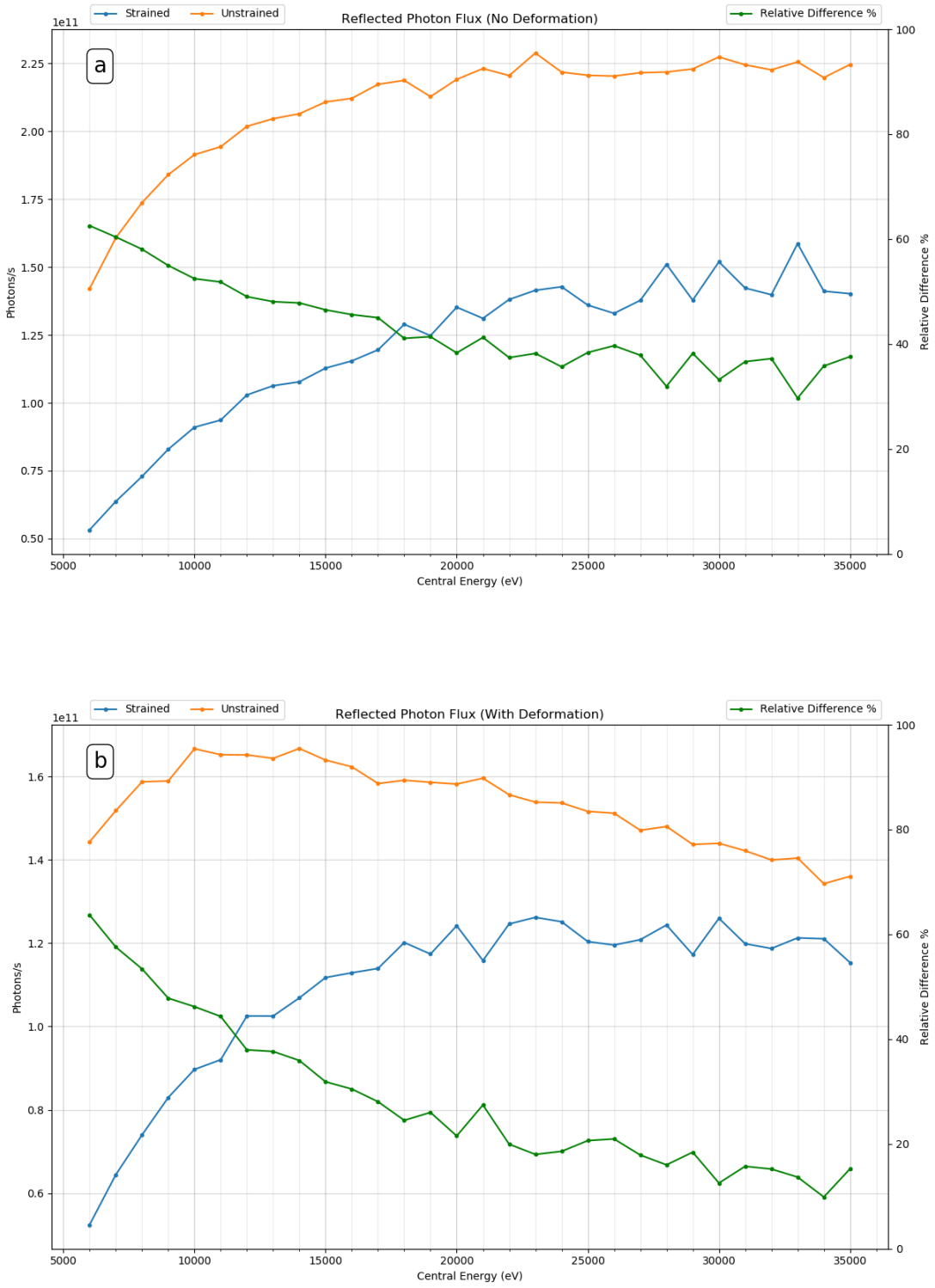

Figure 5.9: Photon flux leaving the Si 333 monochromator with strained and non-strained first crystal (a) ignoring surface deformation, (b) including deformation

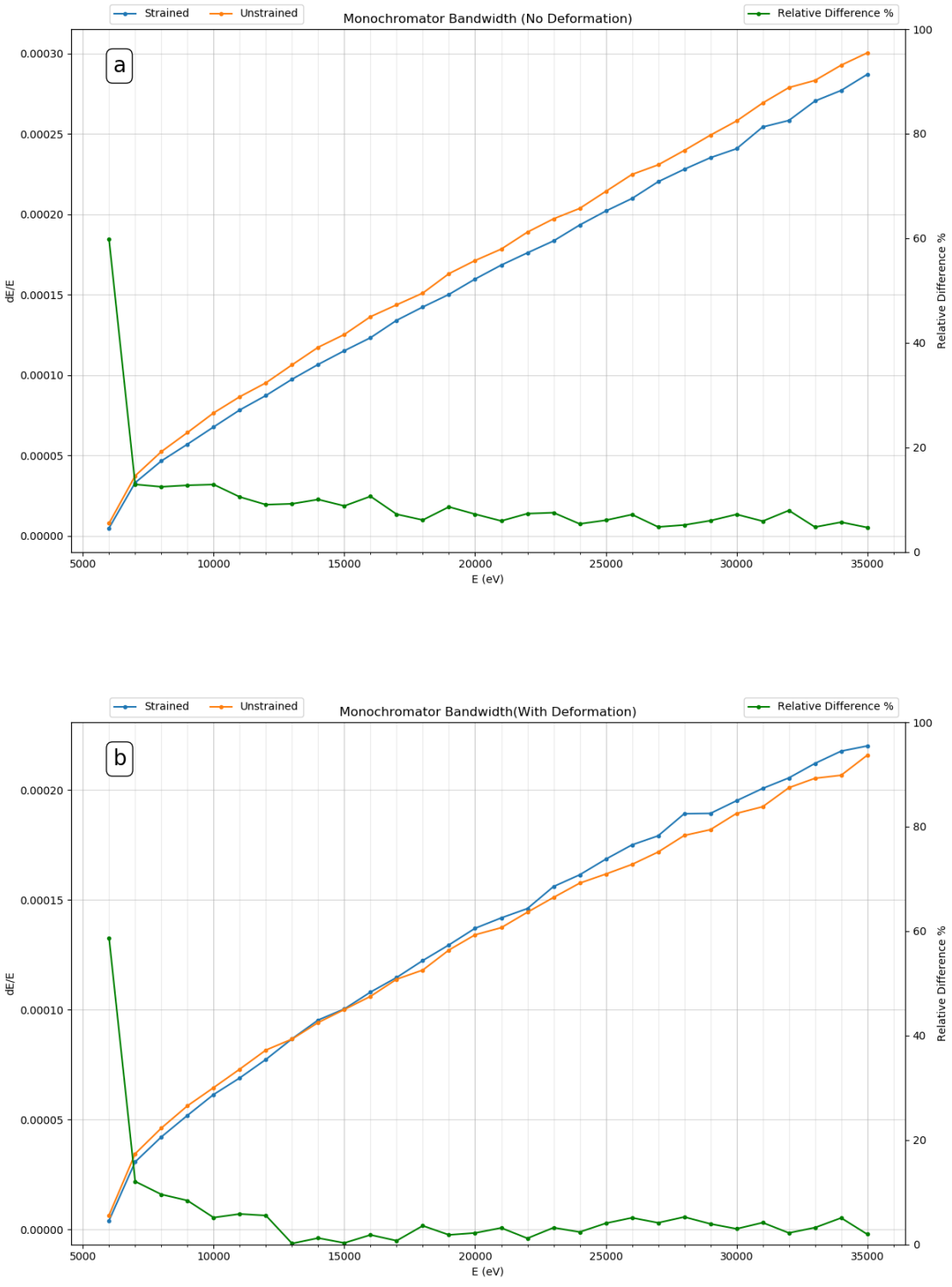

Figure 5.10: Si 333 Monochromator bandwidth (dE/E, standard deviation) with strained and non-strained first crystal (a) ignoring surface deformation, (b) including deformation

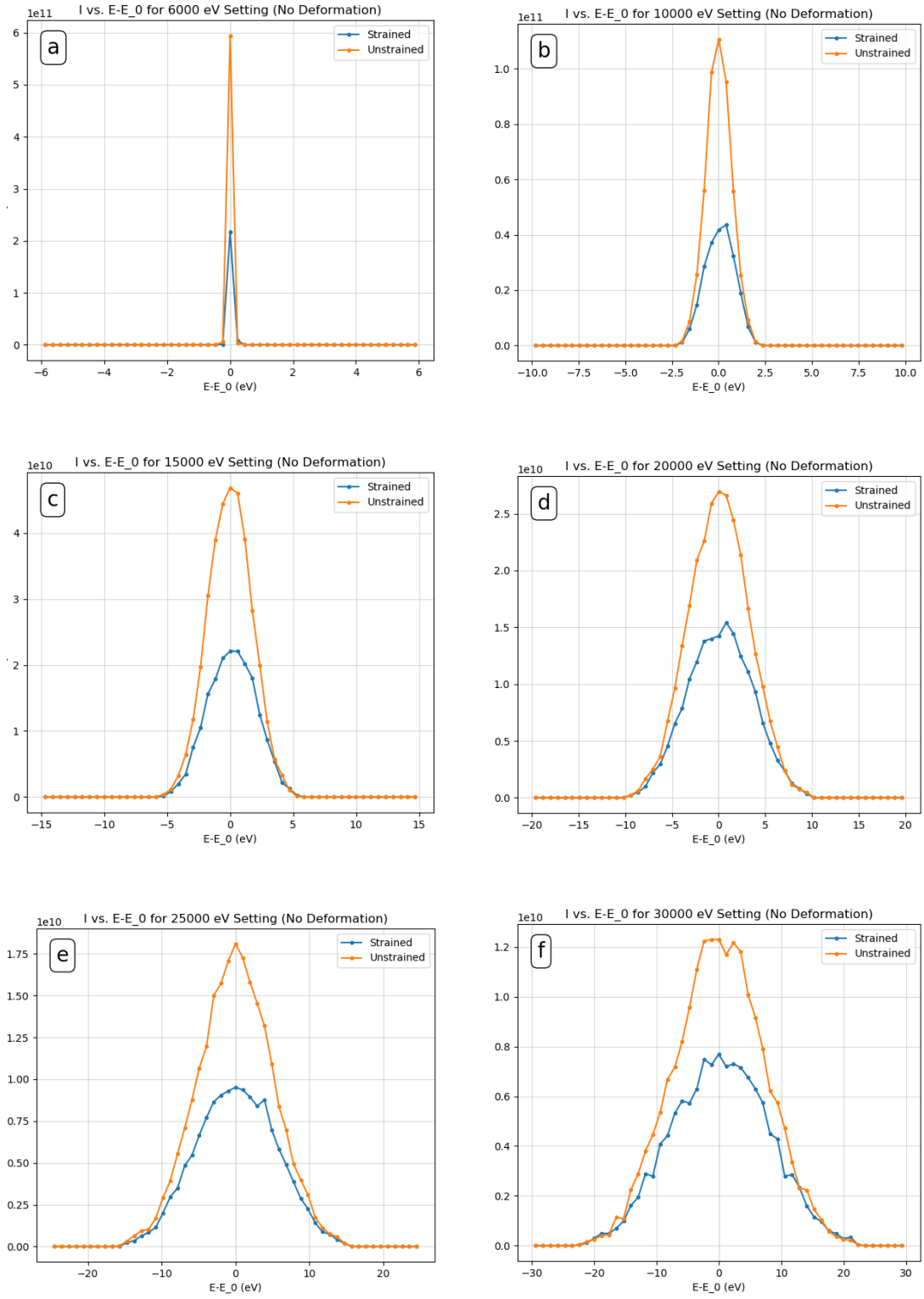

Figure 5.11: Two times Si 333 reflection curves with and without strain at (a) 6 keV, (b) 10 keV, (c) 15 keV, (d) 20 keV, (e) 25 keV, and (f) 30 keV photon energy settings. The y axis is given as photons per second per eV. Surface deformation is not considered.

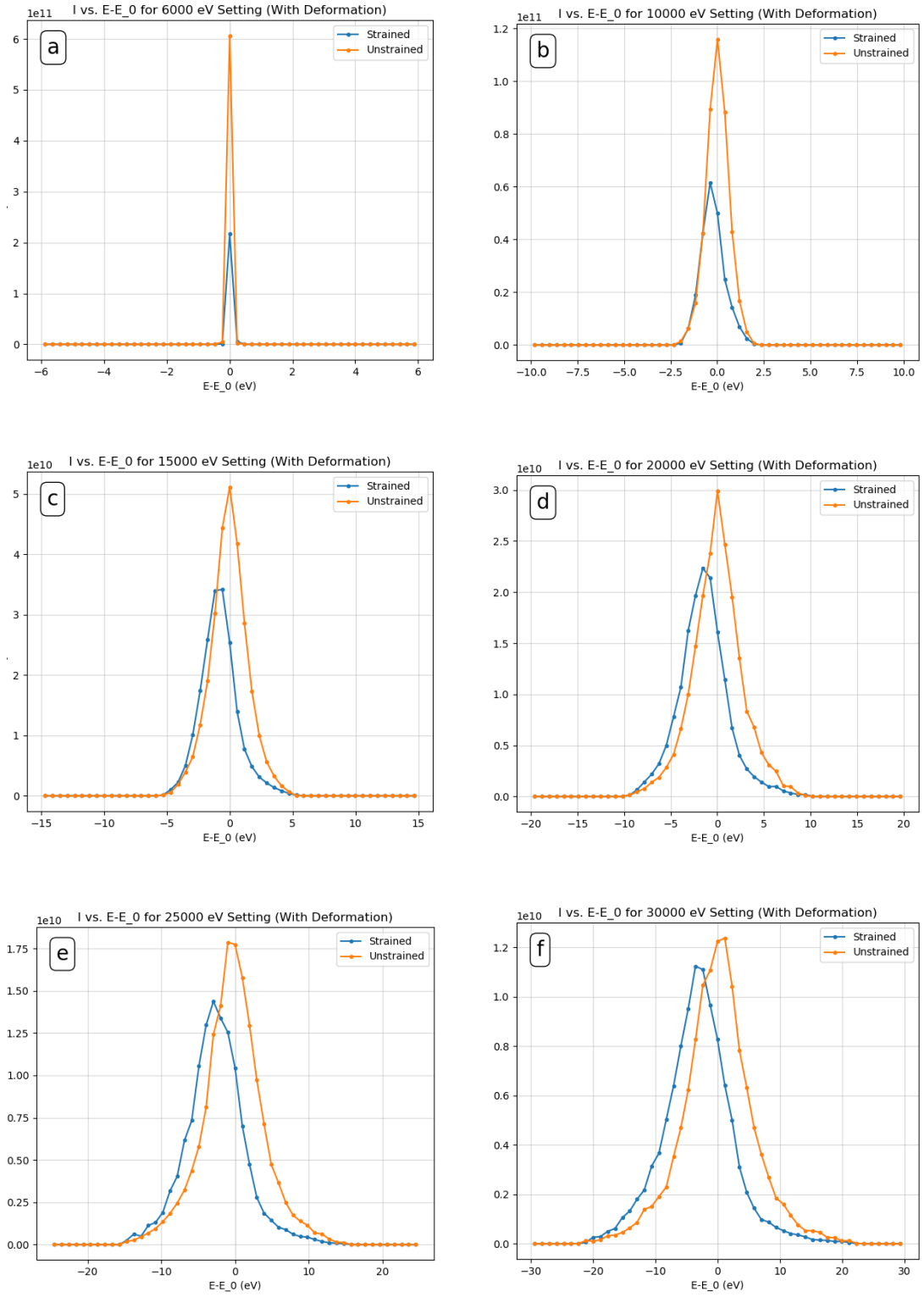

Figure 5.12: Two times Si 333 reflection curves with and without strain at (a) 6 keV, (b) 10 keV, (c) 15 keV, (d) 20 keV, (e) 25 keV, and (f) 30 keV photon energy settings. The y axis is given as photons per second per eV. Surface deformation is considered.

5.5 Power

Flux curves for scan 2, over source powers 50, 100, 150 and 200 Watts are plotted in Figure 5.13. The top 4 lines are results for a Si 333 crystal without considering strain or deformation while the bottom four consider both. The flux is normalized to match that of the 50 W case.

The results clearly show that increases in source power reduce the percentage of the reflected photon flux. This is due to more dramatic strains and deformations at higher power. These effects appear to simply scale the flux curves.

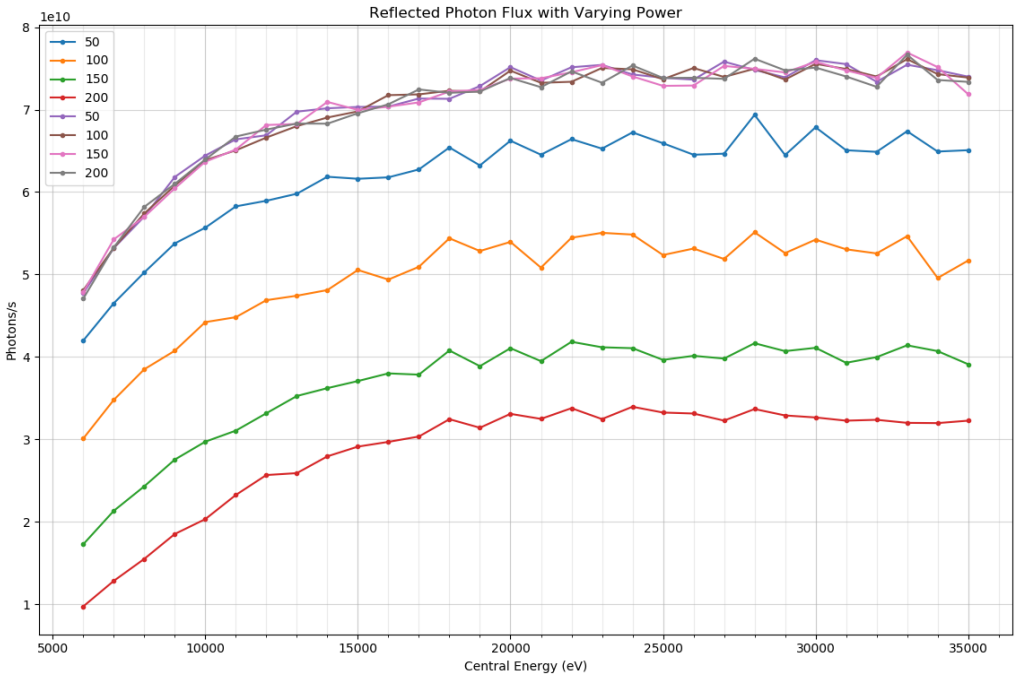

Figure 5.13: Normalized photon flux leaving the Si 333 monochromator for source powers of 50, 100, 150, 200 Watts. The top four lines are without strain or deformation. The bottom four include strain and deformation.

5.6 Source Size

In Figure 5.14 one sees that source size has no significant effect on flux within the range of the scan.

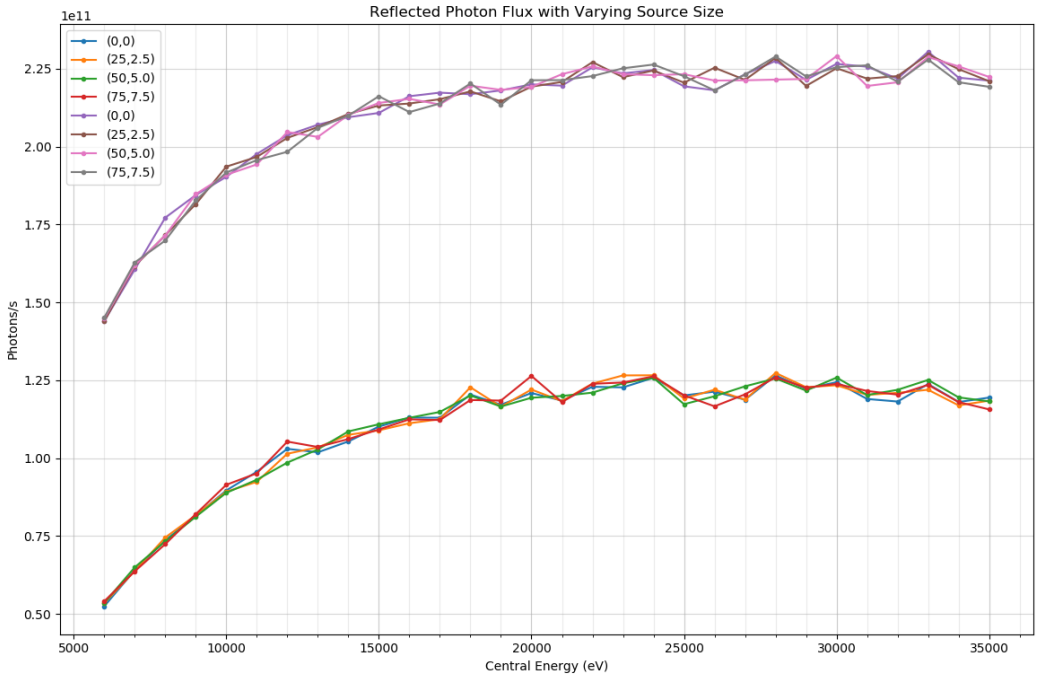

Figure 5.14: Photon flux leaving the Si 333 monochromator for source sizes, (x, z), of (0, 0), (25, 2.5), (50, 5.0), and (75, 7.5) μm^2 is plotted. The top four lines are without strain or deformation. The bottom four include strain and deformation.

5.7 Crystal Distance from Source

Figure 5.15 plots flux curves for varying distances of the first crystal from the source. In the case of the jump from 20 to 40 meters there is a large change in flux. This is due to the decrease of power per unit area and resulting reduction in strain and deformation. The 80 meter flux curve shows a small drop in flux at higher energies. This is due to the small Bragg angle and the beam footprint extending over the crystal boundaries.

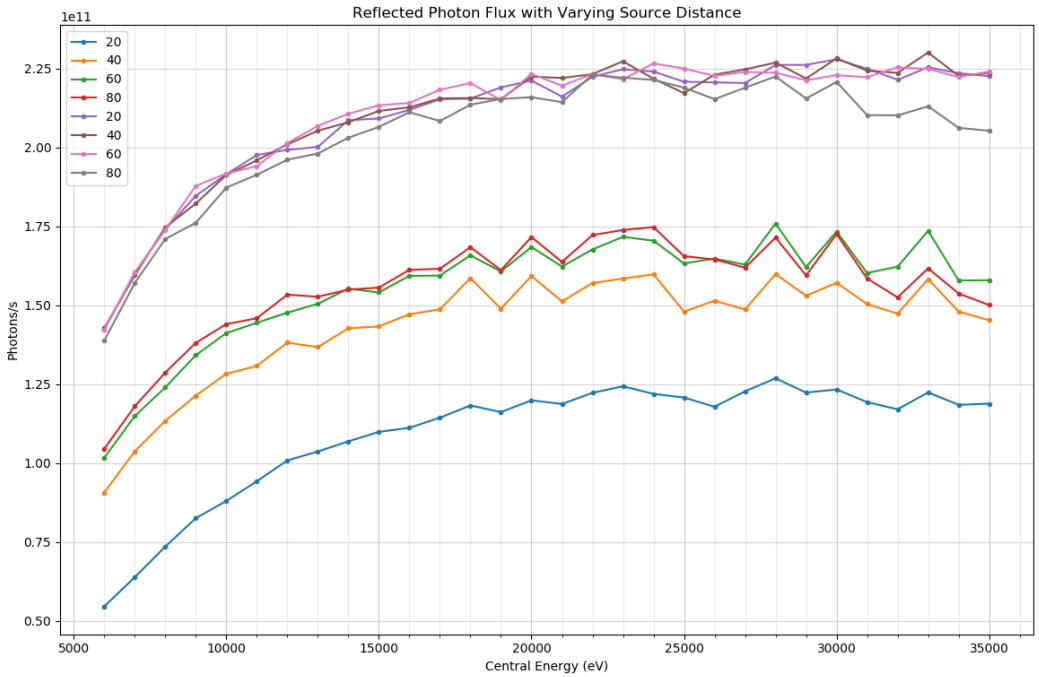

Figure 5.15: Photon flux leaving the Si 333 monochromator for distances of 20, 40, 60, and 80 meters from the source. The top four lines are without strain or deformation. The bottom four include strain and deformation.

5.8 Beam Divergence

It appears from Figure 5.16 that a smaller beam divergence decreases total flux in the first crystal strained and deformed by the heat of the absorbed beam. This is likely due to the smaller divergence having a higher intensity compared to a more divergent beam. It is more interesting to scan divergence while maintaining equivalent intensity on the crystal surface. This study is in planning at the time of this writing.

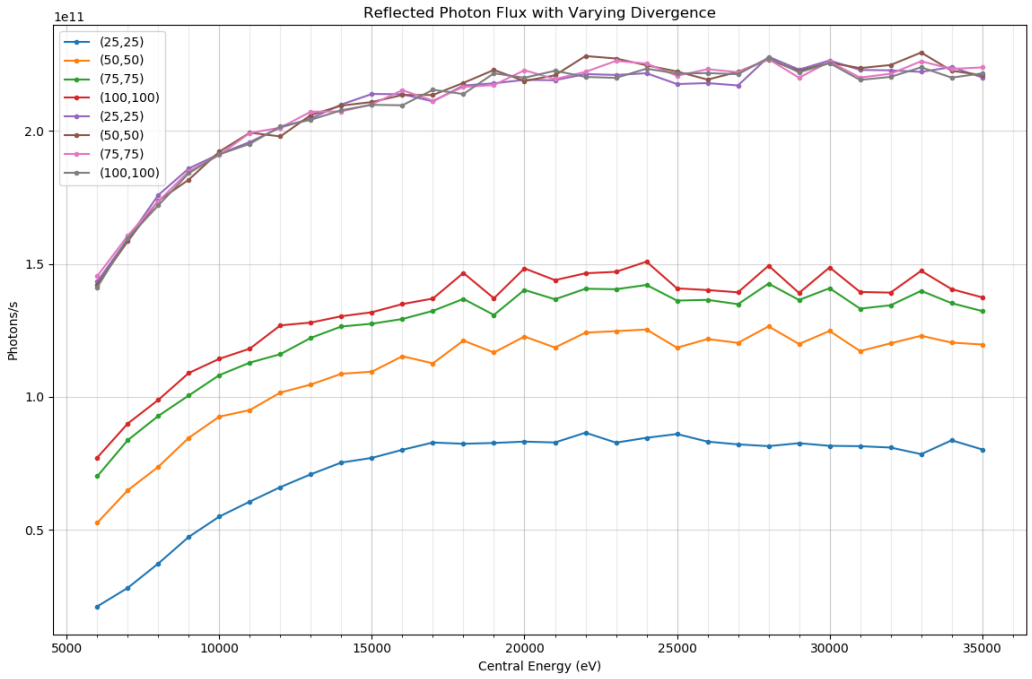

Figure 5.16: Photon flux leaving the Si 333 monochromator with beam divergence, (x_p, z_p), of (25,25), (50,50), (75,75), and (100, 100) in μrad^2. The top four lines are without strain or deformation. The bottom four include strain and deformation.

5.9 NanoMAX and BioMAX Models

Though it was an important goal of the study, the NanoMAX and BioMAX studies were not completed. This was due to time constraints, namely to improve the FEA model and integrate it into MASH.

The model was programmed to solve for fluid flow each time it was run. A simulation with 90 FEA runs at 20 minutes each could take a couple of days. Several of these simulations could take weeks. The future goal is to have a presolved fluid flow. This would reduce the FEA computation time by an estimated factor of 4.

6 Outlook

A thorough investigation into the effects of strain in silicon monochromators in modern synchrotron hard X-ray beamlines has begun. It is now considered that crystal strain can have a significant impact on monochromator reflectivity. There is much work remaining in order to elucidate the effect fully. For example, investigating other sources such as undulators and wigglers which may provide more tangible quantitative results. Specific monochromator setups such as the NanoMAX and BioMAX monochromator are also worth investigating. The attenuating effects on low divergence light sources is of particular importance in studying the highly brilliant beams at the MAX IV facility.

In that respect it is required to compare the FEA models to in situ measurements of crystal monochromators. Do the crystal temperatures match those in the FEA? Does the deformation compare to what is found in simulation? Is there mechanical stress from the monochromator mounting that must be considered in the simulation? Perhaps there is a crystal temperature that best preserves the beam. Can a cooling system be designed to maintain this temperature? All these questions lead to challenging experimentation. However, a machine with so much potential should be stretched to the ends of its capabilities. Improving beam quality is the perennial quest of all synchrotron radiation scientists.

A detailed design report for the beamline ForMAX is in its early stages and is to be completed late 2018. The analyses that began in this study will continue by modeling the planned ForMAX monochromator, including strain effects, giving better insight into the beamline's capabilities.

Further experimentation, as described above, and publication of results are planned.

References

[1] Lin Zhang. Thermal deformation of cryogenically cooled silicon crystals under intense x-ray beams: measurement and finite-element predictions of the surface shape. *J. of Synchrotron Radiat.*, 20:567–580, 2013.

[2] Philip Willmott. *An Introduction to Synchrotron Radiation Techniques and Applications*. Wiley, 2011.

[3] CERN Courier. MAX IV paves the way for ultimate x-ray microscope. 2016. http://cerncourier.com/cws/article/cern/65818.

[4] Ulf Johansson, Ulrich Vogt, Anders Mikkelsen. NanoMAX: a hard x-ray nanoprobe beamline at MAX IV. *Proc. SPIE*, 8851:8851 – 8851 – 10, 2013.

[5] BioMAX. https://www.maxiv.lu.se/accelerators-beamlines/beamlines/biomax/.

[6] ForMAX. https://www.maxiv.lu.se/accelerators-beamlines/beamlines/formax/.

[7] MAX IV. MAX IV - we make the invisible visible. 2018. https://www.maxiv.lu.se/.

[8] Lawrence Berkeley Laboratory. Bend magnet spectrum, 2018. http://henke.lbl.gov/.

[9] National Synchrotron Radiation Research Center. http://www.nsrrc.org.tw.

[10] SPring-8, 2018. http://www.spring8.or.jp/en.

[11] James A. Clarke. *The Science and Technology of Undulators and Wigglers*. Oxford Science Publications, 2004.

[12] Manuel Sanchez del Rio. Shadow3: a new version of the synchrotron x-ray optics modelling package. *J. of Synchrotron Radiat.*, 18:708–716, 2011.

[13] COMSOL Multiphysics® . *version 5.3a*.

[14] MATLAB. *version 8.3.0.532 (R2014a)*. The MathWorks Inc., Natick, Massachusetts, United States, 2014. https://www.mathworks.com.

[15] Peter Sondhauss. MASH, a framework for the automation of x-ray optical simulations. *Proc. SPIE*, 9209:92090C–1, 2014.

[16] F.N. Chukhovskii. The dynamical theory of x-ray bragg diffraction from a crystal with a uniform strain gradient. the Green-Riemann functions. *Acta Cryst.*, A34:610–621, 1978.

[17] D. Taupin. Théorie dynamique de la diffracion des rayons x par les cristaux déformés. *Bull. Soc. franc Minér. Crist.*, 87:469–511, 1964.

[18] Peter Sondhauss. Metal-like heat conduction in laser-excited InSb probed by picosecond time-resolved x-ray diffraction. *Physical Review B*, 78, 2008.

[19] Python. *version 3.6.5*. Python Software Foundation, Delaware, United States, 2018. https://www.python.org.

A Abbreviations

BPM	beam position monitor
CAD	computer-aided design
FEA	finite element analysis
LINAC	linear accelerator
RANS	Reynolds-averaged Navier-Stokes
USG	Uniform Strain Gradient

B FEA Parameters

This appendix tabulates parameter values for materials in simulations.

Silicon

Parameter	Value	Units	Description
h	0.3	W/cm^2·K	Heat transfer coefficient
T_{cool}	77	K	Side cooling temperature
C_{11}	1.6772×10^{11}	Pa	Stiffness tensor 11 component
C_{12}	6.4980×10^{10}	Pa	Stiffness tensor 12 component
C_{44}	8.0360×10^{10}	Pa	Stiffness tensor 44 component
C_p	0.2	J/g·K	Heat capacity at constant pressure
ρ	2329	kg/m^3	Density

Copper

Parameter	Value	Units	Description
C_p	385	J/kg·K	Heat capacity at constant pressure
κ	400	W/m·K	Thermal conductivity
ρ	8960	kg/m^3	Density

Indium

Parameter	Value	Units	Description
C_p	233	J/kg·K	Heat capacity at constant pressure
κ	81.6	W/m·K	Thermal conductivity
ρ	7290	kg/m^3	Density

Liquid Nitrogen

Parameter	Value	Units	Description
μ	157.9×10^{-6}	Pa·s	Dynamic viscosity
γ	1.47	1	Ratio of specific heats
C_p	2.04	kJ/kg·K	Heat capacity at constant pressure
κ	139.6	mW/m·K	Thermal conductivity
ρ	0.807	g/ml	Density

Acknowledgements

This writing was quite the effort. But it was not all my own! Peter Sondhauss dedicated many hours (even on the weekend!) to helping me succeed. He's a really great guy and I give him so much thanks!

Thanks also to Sverker Werin for his supervision and kind check ups on us students. And to Teresia Olsson for similar persistence in augmenting our learning as a teacher's assistant. I appreciate the teaching of Rajmund Mokso and Gunnar Öhrwall and the enthusiasm they've shared with me.

Thanks to the kind MAX IV staff especially Robin Ollivander, who always waves as I walk by and opens the door automatically for me from behind his desk, and Lisbeth Olsson whose laughter fills the halls. And to whoever brings us all the good fruit to eat. Also, Anders Holmström the funny guy who is not only a great help with computers but fun to see around. Thanks to Emilie Hilner, a cool boss who has a calming and down-to-earth presence. And to everyone else I talk to, not one of which unkind.

I am very thankful to the friends in my program Georgía Paraskáki, Georgi Georgiev, and Mohammed Ebbeni who have made the time here so fun. And those moving on I will miss very much.

Thanks to everyone I've met in Lund who have been nothing but supportive of my hopes and aspirations here and for welcoming me to this new country. And a huge thanks to Lund University for all it does to remain an endless source of intellectual wealth for its students and the world around.

Last but not least, I send a loving thanks to my entire family who always encouraged my efforts towards education, even if it meant traveling to the other side of the world for it. And especially to my grandma and uncle who believed in me since day one.